

NASA Technical Memorandum 87247

NASA-TM-87247 19860015398

Criteria for Significance of Simultaneous Presence of Both Condensible Vapors and Aerosol Particles on Mass Transfer (Deposition) Rates

Süleyman A. Gökoğlu
*Lewis Research Center
Cleveland, Ohio*

February 1986

LIBRARY COPY

APR 4 1986

LANGLEY RESEARCH CENTER
LIBRARY, NASA
HAMPTON, VIRGINIA



NF01505

NASA

CRITERIA FOR SIGNIFICANCE OF SIMULTANEOUS PRESENCE OF BOTH
CONDENSIBLE VAPORS AND AEROSOL PARTICLES
ON MASS TRANSFER (DEPOSITION) RATES

Süleyman A. Gökoğlu*
National Aeronautics and Space Administration
Lewis Research Center
Cleveland, Ohio 44135

ABSTRACT

The simultaneous presence of aerosol particles and condensible vapors in a saturated boundary layer may affect deposition rates to subcooled surfaces because of vapor-particle interactions. Scavenging of condensible vapors by aerosol particles may lead to increased particle size (and mass) and decreased vapor mass fraction, thus altering both vapor and particle deposition rates. Particles, if "sufficiently" concentrated, may also coagulate. Criteria are provided here to assess the significance of such phenomena when particles are already present in the mainstream and are not created inside the boundary layer via homogeneous nucleation. It is determined that there is direct proportionality with (a) the mass concentration, $(\rho\omega)$, of both condensible vapors and aerosol particles, and (b) the square of the boundary layer thickness to particle diameter ratio, $(\delta/d_p)^2$. Inverse proportionality was found for mainstream to surface temperature difference, ΔT , if thermophoresis dominates particle transport. A numerical example is worked out for a coal fired PFBC turbine application obtained from the literature. It is concluded that $(\delta/d_p)^2$ is the single most critical factor to consider in deciding when to neglect vapor-particle interactions.

*Case Western Reserve University, Department of Mechanical and Aerospace Engineering, Cleveland, Ohio 44106 and NASA Resident Research Associate.

86N24869

NOMENCLATURE

c_p	specific heat at constant pressure per unit mass of mixture
D	Brownian (Fick) diffusion coefficient (mass diffusivity)
Da	Damköhler number, Eq. (12)
d_p	particle mean diameter
j''	diffusional mass flux
k	Boltzmann constant
Le	Lewis number, Pr/Sc
Ma	Mach number
Nu	Nusselt number for heat or mass transfer
Pr	Prandtl number
p	pressure
R	nose radius of turbine blade
Re_R	Reynolds number based on blade nose radius
\dot{r}''	local rate of vapor consumption, Eq. (1)
Sc	Schmidt number
T	absolute temperature
t	characteristic time
U_∞	turbine inlet ("approach") velocity
u, v	fluid velocity in x and y directions parallel and normal to wall, respectively
v_T	thermophoretic velocity, Eq. (3)
x, y	distance along and normal to the surface
α	thermal (heat) diffusivity of carrier gas mixture, $\lambda/(\rho c_p)$
α_T	thermal diffusion factor, Eq. (3)
B	binary coagulation rate constant, Eq. (14)
δ	boundary layer thickness
λ	thermal conductivity of mixture

- μ viscosity of mixture
- ν kinematic viscosity (momentum diffusivity) of mixture, μ/ρ
- ρ density
- ω mass fraction in prevailing mixture

Subscripts

- h heat transfer
- i condensible vapor species
- m mass transfer
- max maximum
- p particle
- r reaction, Eq. (11)
- T thermophoresis
- w at the surface (wall)
- ∞ upstream infinity

Miscellaneous

- Δ difference operator

INTRODUCTION

The performance deterioration of many different types of high temperature systems is closely related to the diffusion rates of reactants, reaction intermediates, reaction products, and impurities. Energy conversion device manufacturing as applied to aeronautics and/or power plants, and chemical synthesis reactors as applied to high technology materials processing (e.g., CVD techniques for microelectronic circuitry) are examples of such systems where deposition (via diffusion) is suppressed or exploited to avoid efficiency degradation or to improve product quality and life.

Often both aerosol particles and condensible vapors experiencing steep temperature gradients are present in these systems. Here, we consider only sufficiently small particles that are incapable of inertially impacting on

deposition surfaces under the prevailing aerodynamic conditions. The recent studies of Ahluwalia and Im (1,2), Nadkarni and Mahalingham (3), and Castillo and Rosner (4,5) deal with the effects of having the simultaneous presence of vapors and particles and allowing for condensation in (super)saturated mainstreams and/or boundary layers. It has been shown that the mutual interaction of vapors and particles has interesting total (and individual) deposition rate consequences and can significantly alter predicted behavior obtained from "pure" treatments alone.

Small particle transport in temperature gradients is dominated by thermophoresis (particle drift down a local temperature gradient) (6-9). Vapors, on the other hand, are transported primarily by Fick diffusion down local concentration gradients. Although under the prevailing thermodynamic conditions the supersaturation of the condensible vapors may not be sufficient to overcome the kinetic barriers for homogeneous nucleation, when both particles and vapors coexist in a system, particles can serve as possible nucleation sites for vapors. Vapors can be scavenged by condensation on the surface of particles. Moreover, if the particle concentrations and/or residence times inside the boundary layer are large enough, the particles may coagulate (agglomerate).

The objective of this study is to provide a fast estimation method for a design engineer to assess the significance of (a) the influence of the presence of condensible vapors on particle deposition rates, (b) the influence of the presence of particles on vapor deposition rates, and (c) the influence of coagulation on particle deposition rates, under conditions where the particles are already present in the mainstream and are not created inside the boundary layer via homogeneous nucleation. An example case is provided for a typical coal-fired pressurized-fluidized bed combustor (PFBC) power plant as obtained from Refs. 10 and 11. Note that the intention is to be able to

quickly decide when to safely ignore the effects of above-mentioned phenomena. The reader is referred to Refs. 1 to 5 if such effects can not be neglected.

ANALYSIS

The boundary layer conservation equations for condensible vapor species and small aerosol particles, even with such simplifying assumptions as incompressible flow, constant (temperature independent) thermodynamic and transport properties, very dilute species in the host gas ($\omega_i, \omega_p \ll 1$), and monodisperse aerosols, are coupled and have to be solved simultaneously. Thermophoresis dominates diffusion because even when the deposition surface is about 2 percent cooler than the mainstream ($T_w/T_\infty = 0.98$ because of, say, modest conduction and radiation losses with no active cooling), the enhancement of the deposition rate of, say, a $0.1 \mu\text{m}$ particle due to thermophoresis is about an order of magnitude (even higher for larger particles and colder walls) (7). The boundary layer mass conservation equations for the condensible vapor and aerosol particles in two dimensions can then be expressed as:

$$\rho u \frac{\partial \omega_i}{\partial x} + \rho v \frac{\partial \omega_i}{\partial y} = \rho D_i \frac{\partial^2 \omega_i}{\partial y^2} - \dot{r}''' \quad (1)$$

$$\rho u \frac{\partial \omega_p}{\partial x} + \rho(v + v_T) \frac{\partial \omega_p}{\partial y} = -\rho \omega_p \frac{\partial v_T}{\partial y} + \dot{r}''' \quad (2)$$

where v_T is the aerosol particle thermophoretic velocity given by

$$v_T = -\alpha_{T,p} D_p \frac{\partial \ln T}{\partial y} \approx -\alpha_{T,p} D_p \frac{\Delta T}{T_w} \frac{1}{\delta_h} \quad (3)$$

and \dot{r}''' denotes the mass of vapor locally scavenged by the aerosol particles per unit time and volume. If one approximates the shapes of the aerosol particles by spheres, neglects the relative velocity of condensible vapors with respect to aerosol particles, and takes the largest possible mass

transfer driving force, then $(\dot{r}''')_{\max}$ can be expressed in terms of the diffusion flux of the condensible vapors onto the surfaces of aerosol particles, i.e.,

$$(\dot{r}''')_{\max} = \left(\frac{D_1}{d_p} \cdot 2 \cdot \rho \omega_{1,\infty} \right) \cdot \left(\pi d_p^2 \right) \cdot \left[\frac{\rho \omega_{p,\infty}}{\left(\frac{\pi}{6} \right) d_p^3 \rho_p} \right] = 12 \cdot \frac{D_1}{d_p^2 \rho_p} \cdot \rho \omega_{1,\infty} \cdot \rho \omega_{p,\infty} \quad (4)$$

where the mass transfer Nusselt number is taken to be two, corresponding to mass transfer to/from spheres in a quiescent medium. Note that the analysis below will provide a conservative estimate of the significance of the above-mentioned effects because we will use the largest possible reaction (condensation) rate, $(\dot{r}''')_{\max}$. In reality the actual reaction (condensation) rate, \dot{r}''' , will be smaller because (a) the local mass fractions of both condensible vapors, ω_1 , and aerosol particles, ω_p , inside the boundary layer will be smaller than their corresponding mainstream values $\omega_{1,\infty}$ and $\omega_{p,\infty}$, and (b) the driving force for condensation onto the aerosol particle is determined by the difference between the condensible vapor local mass fraction, ω_1 , in the boundary layer and the mass fraction locally prevailing on the aerosol particle surface at the gas/condensate interface (assumed to be much smaller than ω_1 here).

The Effects of The Presence of Condensible Vapors on Particle Deposition Rates

The thermophoretic velocity, v_T , of aerosol particles depends on the thermophoretic diffusivity, $\alpha_{T,p} D_p$, as shown in Eq. (3). However, because the thermophoretic diffusion factor, $\alpha_{T,p}$, is inversely proportional to the Brownian diffusion coefficient, D_p , the thermophoretic velocity is actually independent of D_p (and, hence, d_p) (8). Therefore, it is known a priori that vapors condensing on the aerosol particle surfaces will not affect their thermophoretic velocity. However, the deposition rate of the aerosol particles will still be affected because the depositing particles will be

larger (heavier). A proper way to measure the significance of this effect is to consider the maximum fractional change in the aerosol particle diameter due to vapor condensation. The rate of change of mass of an aerosol particle, $\Delta m/\Delta t$, is given by

$$\frac{\Delta m}{\Delta t} = \rho_p \left(\pi \frac{\Delta (d_p^3)}{6} \right) = \rho_p \pi \frac{d_p^2}{2} \frac{\Delta d_p}{\Delta t} \quad (5)$$

But $\Delta m/\Delta t$ is also given by the mass deposition rate of the saturated vapors condensing on the aerosol particle surface, i.e.,

$$\frac{\Delta m}{\Delta t} = \left(\pi d_p^2 \right) \left(j_i'' \right) = \left(\pi d_p^2 \right) \left(\frac{D_i}{d_p} \cdot 2 \cdot \rho \omega_{i,\infty} \right) \quad (6)$$

Equating Eqs. (5) and (6), and solving for Δd gives

$$\Delta d = 4 \frac{D_i}{d_p} \frac{\rho \omega_{i,\infty}}{\rho_p} \Delta t \quad (7)$$

In Eq. (7), Δt is the residence time of the aerosol particles travelling with a thermophoretic speed $|v_T|$ inside the thermal boundary layer of thickness, δ_h , and can be estimated from

$$\Delta t \approx \frac{\delta_h}{v_T} \approx \frac{\delta_h}{\alpha_{T,p} \frac{D_i}{d_p} \frac{\Delta T}{T_w} \frac{1}{\delta_h}} = \frac{\delta_h^2}{\alpha} \cdot \frac{1}{(\alpha_{T,p} Le_p)} \cdot \frac{T_w}{\Delta T} \quad (8)$$

Combining Eqs. (7) and (8), the fractional change in the aerosol particle diameter is given by

$$\frac{\Delta d_p}{d_p} = 4 \cdot \frac{Le_i}{(\alpha_{T,p} Le_p)} \cdot \frac{T_w}{\Delta T} \cdot \frac{\rho \omega_{i,\infty}}{\rho_p} \cdot \left(\frac{\delta_h}{d_p} \right)^2 \quad (9)$$

The parameters in Eq. (9) can be readily estimated for the prevailing system operating conditions to assess the significance of vapor scavenging by particles (see the example below).

The Effect of The Presence of Aerosol Particles on Vapor Deposition Rates

A measure of the importance of the presence of ash particles acting as sink for vapor molecules can be obtained by comparing the relative magnitude of the reaction (\dot{r}'') term in Eq. (1) to the diffusion term. An effective Damkohler number defined as

$$Da \equiv \frac{\text{characteristic vapor diffusion time across mass transfer boundary layer}}{\text{characteristic reaction (condensation) time}}$$

is such a quantity. The characteristic vapor diffusion time is given by

$$t_d = \frac{\delta_{m,i}^2}{D_i} \quad (10)$$

and, the characteristic reaction (condensation) time is given by

$$t_r = \frac{\rho \omega_{i,\infty}}{(\dot{r}''')_{\max}} = \frac{1}{12} \frac{d_p^2 \cdot \rho_p}{D_i \cdot \rho \omega_{p,\infty}} \quad (11)$$

Therefore,

$$Da = \frac{t_d}{t_r} = 12 \cdot \frac{\rho \omega_{p,\infty}}{\rho_p} \cdot \left(\frac{\delta_{m,i}}{d_p} \right)^2 \quad (12)$$

The quantities in Eq. (12) should be estimated for the prevailing system operating conditions.

The Effect of Particle Coagulation on Aerosol Particle Deposition Rates

Because we assume that aerosol particle transport is dominated by thermophoresis, the residence time of the aerosol particle inside the thermal boundary layer is determined by its thermophoretic velocity. A comparison of the characteristic particle residence time inside the thermal boundary layer to the characteristic coagulation time is a measure of the significance of particle coagulation. If one assumes a nearly monodisperse system with Brownian coagulation, then the ratio of two characteristic times is given by,

$$\frac{t_{\text{thermophoresis}}}{t_{\text{coagulation}}} = \frac{\left(\frac{\delta h}{v_T}\right)}{\left[\frac{\beta \rho_{p,\infty}}{\left(\frac{\pi}{6}\right) d_p^3 \rho_p}\right]^{-1}} = \frac{6}{\pi} \left(\frac{\beta}{d_p \alpha}\right) \left(\frac{1}{\alpha_{T,p} Le_p}\right) \left(\frac{T_w}{\Delta T}\right) \left(\frac{\rho_{p,\infty}}{\rho_p}\right) \left(\frac{\delta h}{d_p}\right)^2 \quad (13)$$

where β is the binary coagulation rate constant given by (12),

$$\beta = \frac{8 kT}{3 \mu} \quad (14)$$

Again, one can readily obtain the quantities required for Eq. (13) for the specific system in question (see also the example below).

AN EXAMPLE CASE

The example case in this study is taken from Refs. 10 and 11 for the Exxon PFBC pilot plant/cascade experiments. The plant operated at 10 atm with a combustion turbine inlet temperature of 871 °C (1144 K). The average particulate mass loading was 58 ppm and the particles had a density of 1.5 g/cm³. The cumulative particle size distribution is shown in Fig. 1 as duplicated from Ref. 10. The mean diameter of the particles can be read from Fig. 1 as about 1.2 μm, corresponding to the cumulative size distribution of 50 percent. Note that this mean diameter, based on particle mass ($\sim d_p^3$) rather than the more appropriate particle surface area (Sauter mean diameter), is assumed to be sufficiently accurate for all practical purposes of this example. When Fig. 3 in Ref. 8 is used as a guide to obtain the ratio of particle thermophoretic diffusivity to carrier gas thermal (heat) diffusivity, $\alpha_{T,p} Le_p$ is estimated to be about 0.2 for the prevailing system conditions. The maximum condensible vapor mass loading will be taken to be around 10 ppm and the condensible vapor will be reasonably assumed to have a Schmidt number of unity in the host combustion product carrier gas which is basically air. The nose radius of the turbine blades used in the

plant was 0.635 cm. We will assume that the surface (wall) temperature of the blade is about 50 K (4 percent) smaller than the turbine inlet temperature due to such losses as radiation, conduction, etc. If one is interested in the deposition rates at the stagnation point region of the blades, the heat and mass transfer Nusselt numbers can be estimated from Ref. 13:

$$Nu_h = \frac{R}{\delta_h} = 0.81 (Re_R)^{1/2} (Pr)^{0.4} = 0.70 Re_R^{1/2} \quad (15)$$

$$Nu_m = \frac{R}{\delta_m} = 0.81 (Re_R)^{1/2} (Sc)^{0.4} = 0.81 Re_R^{1/2} \quad (16)$$

respectively, where the Prandtl number for air is taken to be 0.7. Because it is known that current turbines operate at subsonic velocities, we will assume that the turbine inlet velocity is around 250 m/sec resulting in a Mach number of about 0.4. We can now evaluate Eqs. (9), (12), and (13). The numerical values of each of the required quantities as well as their source references are given in Table I. The calculations show that

$$\frac{\Delta d_p}{d_p} = 3.4 \times 10^{-3}$$

$$Da = 5.8 \times 10^{-4}$$

$$\frac{t_{\text{thermophoresis}}}{t_{\text{coagulation}}} = 4.8 \times 10^{-8}$$

for the example case we have chosen. These values indicate that all three effects considered here can be neglected for this example.

The validity of the assumption that only convective-diffusional mass transport is important and that the inertial effects are absent can now be checked. The dimensionless Stokes number defined as $Stk = (\rho_p d_p^2 U_\infty) / (18 \mu R)$ is a measure of the effect of particle inertia. The calculated Stokes number for this example is 0.103, as compared with the critical Stokes number of 0.125 for cylindrical target geometries above which aerosol particle

deposition (capture) starts to get dominated by inertial impaction. Note that although the example Stokes number is less than the critical Stokes number, it is sufficiently close to make it risky to completely neglect inertial effects. However, inclusion of such effects will result in increased particle speeds, therefore reduced residence times, across the boundary layer thus minimizing the chance of interaction of particles with condensible vapors or with each other. Hence, our conclusion that the simultaneous presence of aerosol particles and condensible vapors in the boundary layer does not affect the total (and/or individual) deposition rate is strengthened further.

CONCLUSIONS

When both aerosol particles and condensible vapors are simultaneously present in a saturated boundary layer, their interaction may affect the individual and/or total deposition rates to subcooled surfaces. Criteria are provided for neglecting the effect of aerosol particle scavenging of condensible vapors on (a) particle deposition rates, and (b) vapor deposition rates; and for neglecting particle coagulation. A numerical example is solved for a typical coal fired PFBC turbine application obtained from the literature. It has been determined on the basis of numerical example that particle coagulation will hardly be a problem for turbine applications.

Examination of Eqs. (9) and (12) reveals that the effect of particle scavenging of condensible vapors depends directly on the mass concentration of condensible vapors ($\rho\omega_{i,\infty}$) and aerosol particles ($\rho\omega_{p,\infty}$), respectively. However, given the fact that the example was for $p = 10$ atm and that the mass fractions were high, it is hard to conceive a real turbine application where the $(\rho\omega)$ products will be an order of magnitude larger than those used in this example. The conservative estimation routine presented here, therefore, allows us to conclude that mass concentrations alone can not be responsible for vapor-particle interactions for turbine applications.

Because most current (and future) turbines are actively cooled (larger ΔT 's), the residence times of the aerosol particles inside the boundary layer are, in fact, much smaller than the example case. This further reduces the vapor-particle interaction effect on deposition rates (see Eq. (9)).

A closer look at Eqs. (9), (12), and (13) shows that the ratio of the boundary layer thickness (note that the momentum, heat, and vapor species mass boundary layer thicknesses are essentially the same for our purposes) to the particle diameter is the most important factor in determining the significance of the scavenging and coagulation phenomena. There may certainly be some cases in turbine applications where $(\delta/d_p)^2$ can be significantly larger than the example case. This would result in nonnegligible $\Delta d_p/d_p$ and/or Da values. Lower mass flowrates (ρU_∞) and trailing edge regions of larger size turbine blades may result in such intolerably thick boundary layers. Similarly, particle diameters may very well be smaller than, say, $0.1 \mu\text{m}$ leading to large vapor condensation rates on existing aerosol particle surfaces. This observation is especially important if the boundary layer supersaturation is so large that homogeneous nucleation (not treated here), may initiate, because the resulting particle diameters from homogeneous nucleation are usually between 0.01 to $0.1 \mu\text{m}$, leading to significant vapor-particle couplings. The reader is referred to Refs. 1 to 5 for the treatment of such coupled transport phenomena.

Finally, one should note that the analysis presented here applies also to turbulent boundary layers as long as thermophoresis is the dominant particle transport mechanism or the analysis can easily be extended to turbulent boundary layers using the same concepts but substituting turbulent momentum, heat, and mass diffusivities.

REFERENCES

1. Ahluwalia, R.K. and Im, K.H., "MHD Heat and Seed Recovery Technology Project," ANL/MHD-83-1, Argonne National Laboratory, 1983.
2. Ahluwalia, R.K. and Im, K.H., "Mass Transfer of Trace Species from Superheated Stream to a Subcooled Surface," International Journal of Heat and Mass Transfer, Vol. 28, No. 11, Nov. 1985, pp. 2061-2070.
3. Nadkarni, A.R. and Mahalingam, R., "Aerosol Behavior in Temperature and Concentration Gradient Fields in Nonisothermal Tube Flow," AIChE Journal, Vol. 31, No. 4, Apr. 1985, pp. 603-614.
4. Castillo, J.L. and Rosner, D.E., "Theory of Surface Deposition from Unary Dilute Vapor-Containing Stream Allowing for Condensation within the Laminar Boundary Layer," submitted to Chemical Engineering Science, 1985.
5. Castillo, J.L. and Rosner, D.E., "Theory of Surface Deposition from Particle Laden Dilute, Saturated Vapor-Containing Streams, Allowing for Particle Thermophoresis and Vapor Scavenging within the Laminar Boundary Layer," submitted to Chemical Engineering Science, 1985.
6. Gököçlü, S.A. and Rosner, D.E., "Thermophoretically Augmented Mass Transfer Rates to Solid Walls Across Laminar Boundary Layers," AIAA Journal, Vol. 24, No. 1, Jan. 1986, pp. 172-179.
7. Gököçlü, S.A. and Rosner, D.E., "Thermophoretically-Enhanced Mass Transport, Rates to Solid and Transpiration-Cooled Walls Across Turbulent (Law-of-the-Wall) Boundary Layers," Industrial and Engineering Chemistry Fundamentals, Vol. 24, No. 2, May 1985, pp. 208-214.
8. Rosner, D.E. and Fernandez de la Mora, J., "Small Particle Transport Across Turbulent Nonisothermal Boundary Layers," Journal of Engineering for Power, Vol. 104, No. 4, Oct. 1982, pp. 885-894.

9. Gökoğlu, S.A. and Rosner, D.E., "Correlation of Thermophoretically-Modified Small Particle Diffusional Deposition Rates in Forced Convection Systems with Variable Properties, Transpiration Cooling and/or Viscous Dissipation," International Journal of Heat and Mass Transfer, Vol. 27, No. 5, May 1984, pp. 639-645.
10. Wenglarz, R.A., "An Assessment of Deposition in PFBC Power Plant Turbines," Journal of Engineering for Power, Vol. 103, No. 3, July 1981, pp. 552-560.
11. Nutkis, M.S., Bertrand, R.R., and Loughnane, M.D., "Hot Corrosion/Erosion Testing of Materials for Application to Advanced Power Conversion Systems Using Coal Derived Fuels," EXXON Monthly Technical Report No. 32, Dec. 1978. (DOE Contract No. EX-76-C-01-2452)
12. Friedlander, S.K., Smoke, Dust, and Haze: Fundamentals of Aerosol Behavior, John Wiley & Sons, New York, 1977.
13. Kays, W.M. and Crawford, M.E., Convective Heat and Mass Transfer, Second Edition, McGraw Hill, New York, 1980.
14. Weast, R.C., CRC Handbook of Chemistry and Physics, 59th Edition, CRC Press, Inc., Boca Raton, FL, 1979.

TABLE I.

Symbol	Value	Source
C_p	0.2787 cal/gr-K	Ref. 14
d_p	1.2 μm	Ref. 10
k	1.38×10^{-23} J/K	Ref. 14
$Le_i = Pr/Sc_i$	0.7	Calculated
Ma	0.4	Assumed
Nu_h	229	Calculated
Nu_m	265	Calculated
p	10 atm	Ref. 10
Pr	0.7	Ref. 14
R	0.635 cm	Ref. 10
$Re_R = (\rho U_\infty R)/\mu$	1.07×10^5	Calculated
Sc_i	1	Assumed
T_∞	1144 K	Ref. 10
ΔT	50 K	Assumed
T_w	1094 K	Calculated
U_∞	250 m/sec	Calculated
$\alpha = \lambda/(\rho c_p)$	0.21 cm^2/sec	Calculated
$\alpha_{T,p}^{Le_p}$	0.2	Ref. 8
$\beta = (8 k T_\infty)/(3 \mu)$	9.2×10^{-11} cm^3/sec	Calculated
δ_h	27.7 μm	Calculated
δ_m	24.0 μm	Calculated
λ	179×10^{-6} cal/cm-sec-K	Ref. 14
μ	460×10^{-6} gr/cm-sec	Ref. 14
ρ	3.1×10^{-3} gr/cm ³	Ideal gas law
ρ_p	1.5 gr/cm ³	Ref. 10
$\omega_{i,\infty}$	10 ppm	Assumed
$\omega_{p,\infty}$	58 ppm	Ref. 10

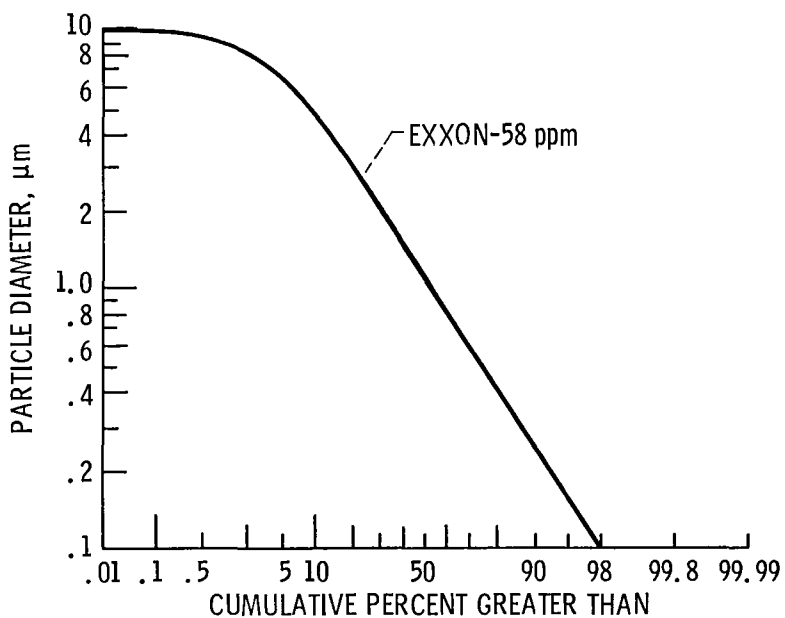


Fig. 1. - Size distribution for 10:1 pressure ratio turbine.

1. Report No. NASA TM-87247		2. Government Accession No.		3. Recipient's Catalog No.	
4. Title and Subtitle Criteria for Significance of Simultaneous Presence of Both Condensible Vapors and Aerosol Particles on Mass Transfer (Deposition) Rates				5. Report Date February 1986	
				6. Performing Organization Code 505-63-11	
7. Author(s) Süleyman A. Gökoğlu				8. Performing Organization Report No. E-2929	
				10. Work Unit No.	
9. Performing Organization Name and Address National Aeronautics and Space Administration Lewis Research Center Cleveland, Ohio 44135				11. Contract or Grant No.	
				13. Type of Report and Period Covered Technical Memorandum	
12. Sponsoring Agency Name and Address National Aeronautics and Space Administration Washington, D.C. 20546				14. Sponsoring Agency Code	
15. Supplementary Notes Süleyman A. Gökoğlu, Case Western Reserve University, Dept. of Mechanical and Aerospace Engineering, Cleveland, Ohio 44106 and NASA Resident Research Associate.					
16. Abstract <p>The simultaneous presence of aerosol particles and condensible vapors in a saturated boundary layer may affect deposition rates to subcooled surfaces because of vapor-particle interactions. Scavenging of condensible vapors by aerosol particles may lead to increased particle size (and mass) and decreased vapor mass fraction, thus altering both vapor and particle deposition rates. Particles, if "sufficiently" concentrated, may also coagulate. Criteria are provided here to assess the significance of such phenomena when particles are already present in the mainstream and are not created inside the boundary layer via homogeneous nucleation. It is determined that there is direct proportionality with (a) the mass concentration, ($\rho\omega$), of both condensible vapors and aerosol particles, and (b) the square of the boundary layer thickness to particle diameter ratio, $(\delta/d_p)^2$. Inverse proportionality was found for mainstream to surface temperature difference, ΔT, if thermophoresis dominates particle transport. A numerical example is worked out for a coal fired PFBC turbine application obtained from the literature. It is concluded that $(\delta/d_p)^2$ is the single most critical factor to consider in deciding when to neglect vapor-particle interactions.</p>					
17. Key Words (Suggested by Author(s)) Vapor deposition; Particle deposition; Gas turbines; Mass transfer; Boundary layers; Aerosols			18. Distribution Statement Unclassified - unlimited STAR Category 31		
19. Security Classif. (of this report) Unclassified		20. Security Classif. (of this page) Unclassified		21. No. of pages	22. Price*

End of Document

DOE/NASA/50112-63
NASA TM-87250

NASA-TM-87250

19860011070

Alloy Chemistry and Microstructural Control to Meet the Demands of the Automotive Stirling Engine

Joseph R. Stephens
National Aeronautics and Space Administration
Lewis Research Center

LIBRARY COPY

MAY 19 1986

LANGLEY RESEARCH CENTER
LIBRARY, NASA
HAMPTON, VIRGINIA



NF01506

Work performed for
U.S. DEPARTMENT OF ENERGY
Conservation and Renewable Energy
Office of Vehicle and Engine R&D

Prepared for
MiCon 1986
sponsored by American Society for Testing Materials
Philadelphia, Pennsylvania, May 15-16, 1986

DISCLAIMER

This report was prepared as an account of work sponsored by an agency of the United States Government. Neither the United States Government nor any agency thereof, nor any of their employees, makes any warranty, express or implied, or assumes any legal liability or responsibility for the accuracy, completeness, or usefulness of any information, apparatus, product, or process disclosed, or represents that its use would not infringe privately owned rights. Reference herein to any specific commercial product, process, or service by trade name, trademark, manufacturer, or otherwise, does not necessarily constitute or imply its endorsement, recommendation, or favoring by the United States Government or any agency thereof. The views and opinions of authors expressed herein do not necessarily state or reflect those of the United States Government or any agency thereof.

Printed in the United States of America

Available from

National Technical Information Service
U.S. Department of Commerce
5285 Port Royal Road
Springfield, VA 22161

NTIS price codes¹

Printed copy: A02

Microfiche copy: A01

¹Codes are used for pricing all publications. The code is determined by the number of pages in the publication. Information pertaining to the pricing codes can be found in the current issues of the following publications, which are generally available in most libraries: *Energy Research Abstracts (ERA)*; *Government Reports Announcements and Index (GRA and I)*; *Scientific and Technical Abstract Reports (STAR)*; and publication, NTIS-PR-360 available from NTIS at the above address.

DOE/NASA/50112-63
NASA TM-87250

Alloy Chemistry and Microstructural Control to Meet the Demands of the Automotive Stirling Engine

Joseph R. Stephens
National Aeronautics and Space Administration
Lewis Research Center
Cleveland, Ohio 44135

Work performed for
U.S. DEPARTMENT OF ENERGY
Conservation and Renewable Energy
Office of Vehicle and Engine R&D
Washington, D.C. 20545
Under Interagency Agreement DE-AI01-85CE50112

Prepared for
MiCon 1986
sponsored by American Society for Testing Materials
Philadelphia, Pennsylvania, May 15-16, 1986

21912-22541 #

Alloy Chemistry and Microstructural Control to Meet the Demands
of the Automotive Stirling Engine

Joseph R. Stephens
National Aeronautics and Space Administration
Lewis Research Center
Cleveland, Ohio 44135

Abstract

The automotive Stirling engine now under development by DOE/NASA as an alternative to the internal combustion engine, imposes severe materials requirements for the hot portion of the engine. Materials selected must be low cost and contain a minimum of strategic elements so that availability is not a problem. Heater head tubes contain high pressure hydrogen on the inside and are exposed to hot combustion gases on the outside surface. The cylinders and regenerator housings must be readily castable into complex shapes having varying wall thicknesses and be amenable to brazing and welding operations. Also, high strength, oxidation resistance, resistance to hydrogen permeation, cyclic operation, and long-life are required. A research program conducted by NASA Lewis focused on alloy chemistry and microstructural control to achieve the desired properties over the life of the engine. Results of alloy selection, characterization, evaluation, and actual engine testing of selected materials will be presented.

KEY WORDS: Automotive Stirling engine; Alloy chemistry; Microstructure; Creep resistance; Oxidation; Hydrogen permeation; Iron-base alloys

The Department of Energy (DOE) and NASA [1] are currently investigating the Stirling engine as an alternative power source to the internal combustion engine for automotive applications. The Stirling engine (Fig. 1) is an externally heated engine that offers the advantages of high efficiency, low pollution, low noise, and multifuel capability. Hydrogen is used as the working fluid for automotive applications in order to obtain maximum efficiency from the engine. Heat is input to the working fluid by a combustion flame impinging on the outside walls of the tubes containing the hydrogen working fluid. Current engines designed for automotive applications use tubes with a wall thickness of 0.75 mm (3.0 mm i.d. by 4.5 mm o.d.). The thin wall is required to achieve maximum heat input to the hydrogen. However, the tube material must be of sufficient strength to contain the hydrogen, which operates at high pressures and temperatures. Automotive design requirements call for a normal maximum pressure of 15 MPa, with peak pressures reaching 21 MPa during transient conditions. Tube walls are designed for an average temperature of 820 °C, with 870 °C common on the flame side. A further requirement is that the tubes operate for a period of 3500 h, which is approximately equivalent to the 160 000-km (100 000-mile) driving life of an engine.

The tubes currently are heated by direct exposure to a combustion flame fired by gasoline or diesel fuel. Alternative fuels such as alcohol and shale oil derivatives may be considered for future applications. Oxidation and corrosion resistance is one of several criteria for selecting heater-head-tube alloys to withstand the extreme operating requirements of the Stirling engine. A second criterion is the resistance of the tube material to hydrogen permeation so that hydrogen recharging of the engine is required in excess of 6 month intervals. Finally, the creep-rupture strength for 3500 h life is a determining factor in selecting a heater tube alloy. These criteria are

interrelated. For example, excessive scale spalling due to oxidation/corrosion will reduce the tube wall thickness and lead to premature failure caused by the high-pressure hydrogen rupturing the tubes or permeating rapidly through the tube walls. Prototype engines and initial models of experimental automotive engines use N-155 (Multimet) for heater head tubes. However, this iron-base alloy contains 20 percent cobalt, a costly and strategic metal. Efforts are currently under way by NASA [2-7] and the contractors on this program, Mechanical Technology Inc. (MTI) and United Stirling Sweden (USAB), to identify substitutes for N-155. The primary emphasis is on high-strength austenitic iron-base alloys although a limited number of nickel-base superalloys are under consideration. As part of the evaluation of candidate substitute alloys the oxidation and corrosion resistance has been determined for 16 alloys [8]. Hydrogen permeation coefficients have been determined for most of those alloys [9], and strength properties have been measured by creep testing in air [2] and hydrogen [10]. Further, endurance testing in a materials simulator rig and engine testing have been used to characterize selected candidate heater tube alloys [3,6,9].

The purpose of this paper is to describe the effects of alloy chemistry and microstructure on the oxidation/corrosion behavior and resistance to hydrogen permeability of candidate alloys.

Procedure

Materials

Twenty alloys (14 iron base, five nickel base, and one cobalt base) were evaluated for their oxidation and corrosion resistance, hydrogen permeability, and endurance under conditions of temperature and environment anticipated for automotive Stirling engines. The chemical compositions of the alloys are listed in Table 1. All of the alloys are commercially available except AL-EX-20, an experimental alloy supplied by Allegheny Ludlum Steel Company.

Iron-base alloys are the primary candidates for automotive Stirling engine applications because their raw material costs are lower than those for nickel-base and cobalt-base alloys. Nickel-base alloys are considered as possible candidates in the event a less expensive iron-base alloy cannot be identified that will meet all of the requirements of the Stirling engine. Cobalt-base alloys are not under consideration for automotive Stirling engine applications because of the high cost of cobalt, its limited availability, and its status as a strategic material (more than 95 percent of the cobalt used in the United States is imported). However, one cobalt-base alloy (HS-188) was included in this investigation as a comparison with the iron- and nickel-base alloys.

For oxidation testing, test coupons 1.27 by 2.54 cm, and generally 0.8 to 1.6 mm thick, with a 0.3-cm-diameter hanger hole, were cut from the alloy sheet material. For hydrogen permeability and endurance testing the alloys used in this study were obtained commercially in the form of tubing with an outside diameter of 4.5 mm and an inside diameter of 3.0 mm (the size used in current prototype engines). Four of the tubing alloys were weld-drawn and the others were seamless tubing. The weld-drawn alloys were N-155, 19-9DL, Inconel 718(wd) and HS-188.

Stirling Engine Simulator Materials Test Rig

The Stirling engine simulator rig used in this program was designed and fabricated at the NASA Lewis Research Center; it consists primarily of a combustion gas heating chamber (Fig. 2) with auxiliary heating, control, and gas management systems. The rig and its operation have been described in detail [3]. The rig was fired with natural gas for initial ignition and then with diesel fuel throughout the test run. Duplicate oxidation-corrosion test specimens were suspended by platinum wires from the hairpin turns of the tubes shown in Fig. 2. The specimens were heated to the desired 820 °C test

temperature (automotive Stirling engine temperature) by the combustion flame flowing over them. The rig was used primarily as a means of ranking candidate heater-head-tube alloys [3,6,9]. The oxidation-corrosion testing was conducted simultaneously with a 3500-h endurance and permeability run of tubing alloys. An endurance run consisted of a series of 5-h cycles to obtain the required 3500 h of test time to simulate the minimum life of an automotive engine. A typical heating cycle consisted of a 6- to 10-min preheat to get to the operating temperature, a 5-h hold at temperature, and a 1-h cooldown to near room temperature. The change in specific weight $\Delta W/A$ with time t for the oxidation coupons was fitted by least squares [11] to equation (1).

$$\frac{\Delta W}{A} = k_1^{1/2} t^{1/2} - k_2 t \pm \text{SEE} \quad (1)$$

where k_1 is an oxide growth constant comparable to a parabolic oxidation scaling constant, k_2 is an oxide spalling constant, and SEE is the standard error of estimate. An oxidation attack parameter K_a [11] was derived from equation (1) and is defined as

$$K_a = k_1^{1/2} + 10k_2 \quad (2)$$

The original hydrogen pressure in the tubes and the pressure at the end of a 5-h cycle were used to calculate the hydrogen permeability coefficient, ϕ , using the equation:

$$P = P_0^{1/2} - \frac{\phi A P_s T t}{2LVT_s} \quad (3)$$

where

P pressure in closed system, MPa

P_0 original pressure, MPa

A permeated area, cm^3

P_s standard pressure, MPa

T temperature of system, K

t time, sec
L membrane thickness, cm
V volume of system, cm³
T_s standard temperature, K

Results

Stirling Engine Simulator Oxidation and Corrosion Tests

Weight Change. - The alloys could be categorized into four groups on the basis of specific weight change data. Alloys in group I had excellent oxidation and corrosion resistance, and their specific weight change was positive (weight gain) throughout the 3500-h test. Group I comprised the five alloys CG-27, Incoloy 800, HS-188, N-155, and Inconel 718. Three of the alloys, CG-27, Incoloy 800, and HS-188, did not exhibit any significant spalling during testing in the Stirling engine simulator rig. Final average specific weight change (Fig. 3) ranged from 1.4 to 0.17 mg/cm² for CG-27 to Inconel 718, respectively.

A second group of alloys is considered to have relatively good oxidation and corrosion resistance under simulated Stirling engine operating conditions. The five alloys in group II in order of increasing final weight loss are RA-330, Sanicro 31H, Sanicro 32, 12RN72, and 253 MA. Final average specific weight change (Fig. 4) ranged from -0.54 to -6.0 mg/cm² for RA-330 to 253 MA, respectively.

The third group of alloys, 316 stainless steel, W-545, A-286, and Nitronic 40 is considered to have fair to poor oxidation and corrosion resistance on the basis of specific-weight-change-versus-time data. Final average specific weight change (Fig. 5) ranged from -22.8 to -41.8 mg/cm² for 316 stainless steel to Nitronic 40, respectively.

A final group of alloys, consisting of 19-9DL and AL-EX-20, exhibited catastrophic oxidation and corrosion behavior upon rig testing. Spalling

began after only a very short time into the test and excessive weight loss occurred after 500 h of cyclic testing. The tests were terminated before the 3500-h goal because of the unacceptable oxidation and corrosion resistance of these alloys.

Attack parameter K_a . - Oxidation and corrosion weight-change-versus-time data were fitted to the parabolic equation (eq. (1)). For three of the alloys, HS-188, Incoloy 800, and CG-27, where no spalling was observed, the attack parameter was calculated from equation (2) with $k_2 = 0$. The remaining 13 alloys also derived their attack parameters from equation (2) but with values of k_2 included. For alloys 19-9DL, Nitronic 40, and AL-EX-20 the $k_1^{1/2}$ term dropped out so that $K_a = 20k_2t$ was used. Figure 6 is a summary plot of calculated K_a values for the alloys. Values of K_a are plotted on a log scale in decreasing order of oxidation and corrosion resistance based on the highest values of the duplicate specimens. The attack parameter ranged from 0.011 for HS-188 to 12.49 for 19-9DL, or over three orders of magnitude. Examination of the K_a values in Fig. 6 suggested that the alloys could again be categorized into four groups. Group I comprised the alloys HS-188, Sanicro 31H, Inconel 718, Incoloy 800, N-155, CG-27, and RA-330, with K_a ranging from 0.011 for HS-188 to 0.031 for RA-330. Group II comprised the three alloys Sanicro 32, 12RN72, and 253 MA, with K_a values of 0.098, 0.110, and 0.159, respectively. Group III comprised the alloys A-286, W-545, 316 stainless steel, and Nitronic 40, with K_a ranging from 0.370 to 0.659. Group IV comprised AL-EX-20, with a K_a of 4.68, and 19-9DL, with a K_a of 12.49. This grouping was somewhat arbitrary, but corresponded to the previous grouping based on final weight change. The only exception was for RA-330, which experienced a net weight loss and was placed in group II

(Fig. 4) but has a K_a value similar to those for the other five alloys in group I.

X-ray diffraction. - The x-ray diffraction data from the specimen surface after testing are summarized in Table 2 by rank of the alloy in decreasing X-ray intensity. In general, the most oxidation and corrosion resistant alloys formed nearly pure Cr_2O_3 as either the most or secondmost intense oxide. The Cr_2O_3 oxide is listed as a sesquioxide, $d(024) = 0.1818$ nm in Table 2. Because Fe went into solution as Fe_2O_3 , the value of d increased. As the d value approached 0.1839 nm, the oxide became essentially pure Fe_2O_3 . Chromite spinel with a_0 ranging from 0.835 to 0.840 nm also formed on most of the alloys during oxidation and corrosion testing. This chromite spinel appeared to be innocuous. Alloy A-286 showed another spinel with $a_0 = 0.830$ nm along with a lower sesquioxide with $d = 0.1813$ nm, and also NiO was formed. Alloy 19-9DL, which oxidized catastrophically, formed as its two strongest oxides a spinel with $a_0 = 0.840$ nm and the desirable oxide Cr_2O_3 with $d = 0.1821$ nm.

Metallography. - Microstructures of selected alloy specimens after the 3500-h test are shown in Fig. 7. Alloy CG-27 (Fig. 7(a)) had an adherent oxide scale on the specimen surface. Alloy Inconel 718 (Fig. 7(b)) had a thin, adherent oxide scale with a small depletion zone present in this alloy. Sanicro 32 (Fig. 7(c)) formed large voids in the depletion zone. Severe grain boundary attack occurred in W-545 (Fig. 7(d)) and resulted in almost total consumption of the alloy matrix beneath the surface oxide.

Electron microprobe analysis. - Alloy CG-27, a group I alloy, was examined because it had excellent oxidation resistance and contained the least chromium of the 16 alloys tested in the rig. The distribution of the major alloying elements and oxygen in the oxide scale and the adjacent metal substrate of CG-27 (Fig. 8) showed the surface oxide to be rich in iron,

nickel, and to a lesser extent aluminum. Beneath this oxide layer was a thin, continuous oxide layer rich in chromium and titanium. Adjacent to the chromium-rich intermediate scale was an aluminum-rich oxide next to the metal substrate, which exhibited a wide zone of internally oxidized aluminum-rich, and somewhat fewer titanium-rich, protrusions.

Metallographic results for the group III alloy W-545 (Fig. 7(d)) indicated a large surface scale consisting of a porous oxide. Results from electron microprobe analyses (Fig. 9) showed an outer oxide rich in iron, nickel, and chromium. Oxygen had penetrated uniformly into this alloy to a substantial depth. The oxide formed appeared to be rich in nickel with some chromium. Iron was depleted from this area, but discrete areas of molybdenum were observed near the surface. Aluminum and titanium did not appear to enter into the oxidation process of this alloy. The composition of W-545 is similar to that of CG-27 except for the large difference in aluminum content. This suggests that aluminum makes a major contribution to the oxidation resistance of CG-27 and that its low concentration in W-545 may explain the poor oxidation resistance of that alloy.

Stirling Engine Simulator Hydrogen Permeation and Endurance Tests

Hydrogen permeability. - Previous measurements of hydrogen permeation during cyclic testing in the simulator rig [12] indicated that hydrogen loss was rapid through the thin wall tubes of alloy N-155. Hydrogen pressure decay curves are shown in Fig. 10(a) for selected 5 h cycles in an 100 h test. It should be noted that pressure loss is rapid and is most severe for the first 5 h cycle. The slight improvement for the remaining cycles is attributed to the formation of an oxide scale on the exterior surface of the tubes. It was shown previously [13] that a thin (0.02 mm) carbide could form on the tubes internal surface in an engine presumably due to oil leaking into the heater head. This carbide layer resulted in reducing the permeability rate of

hydrogen from the engine. A program was undertaken at NASA Lewis [12] to investigate various dopants such as CO, CO₂, CH₄, etc. to form carbide or oxide surface layers on the tubes internal surfaces to act as a barrier to hydrogen permeability. The effects of 1 vol % CO₂ in hydrogen are shown in Fig. 10(b) for alloy N-155. The results suggest that the oxide that formed on the internal surfaces was effective in reducing hydrogen loss from the tubes. Hydrogen permeability coefficients were calculated from the pressure decay curves using equation (3). Permeability coefficients as a function of rig exposure time are plotted in Figs. 11 to 13 for iron, nickel, and cobalt-base alloys, respectively. For iron-base alloys, hydrogen permeability coefficients vary over two orders of magnitude while for the five nickel-base alloys a variation of about a factor of two is noted. A comparison of the hydrogen permeability coefficients after 250 h testing (since some alloys did not survive much longer) is shown in Fig. 14. In general the nickel-base alloys exhibited lower permeability coefficients than the iron-base alloys. An iron-base alloy, CG-27 was an exception to this general observation.

Endurance testing. - Endurance testing was also conducted on the tube alloys by filling with 15 MPa helium. Since helium did not permeate the tube walls, a constant pressure (stress) was maintained. This test is much more severe than actual engine operation where the mean pressure is near 4 MPa, but does provide an effective method for ranking the strengths of the alloys under simulated engine conditions. A comparison of rupture lives is shown in Fig. 15. Only CG-27 and Pyromet 901 survived the 3500 h test. It should be noted for alloy Inconel 718 that seamless tubing (Inconel 718(a)) had a much longer life than the weld-drawn tubing (Inconel 718(wd)). Cold working of 12RN72 (cw) reduced the rupture life from the standard heat treated condition.

Metallography. - Microstructures of selected alloys are shown in Fig. 16. Alloy CG-27 is shown before and after exposure. The oxide film on

both internal and exterior surfaces is evident for the hydrogen and 1 percent CO₂ containing tube (Fig. 16(a)). Alloy Inconel 625 (Fig. 16(b)) exhibited external scale cracking after cyclic exposure.

Discussion of Results

Some insight into the excellent oxidation and corrosion behavior of CG-27 can be gained from the electron microprobe results. The chromium distribution shows that CG-27 had a chromium-rich oxide layer ranging in thickness from about 3 to 4 μm . The poorer oxidation behavior of group II and III alloys was characterized by chromium-rich oxide layers about 8 μm thick (group II alloys) and from 20 to 35 μm thick (group III alloys) [8]. All 16 alloys studied herein formed Cr₂O₃ chromite spinels as their major oxides. The thin, adherent oxide formed by the group I alloys CG-27 and Incoloy 800 (not shown) is believed to be a major contributor to the oxidation resistance of these alloys.

Further comparison of the alloys characterized by electron microprobe techniques indicated that iron and nickel were present as a thin outer oxide in group I alloys. In contrast, in group II alloys and especially in group III alloys, iron and nickel were observed as thick, discrete areas of oxide that were in some cases ready to spall from the specimen. Evidently in group I alloys the iron and nickel oxides formed early in the 3500-h test, and then oxide formation of the more reactive alloying elements took over the oxidizing process. The thicker oxides and higher spalling rates in particular for group III alloys (specific weight losses of 23 to 42 mg/cm² as compared with little or no weight loss for group I alloys) suggest that iron and nickel oxides formed throughout the 3500-h test.

Particular interest was focussed on the apparent roles of the more reactive oxide-forming alloying elements aluminum and titanium contained in some of the alloys. In CG-27 internal oxidation of aluminum to a depth of

approximately 10 μm below the oxide-metal interface was evident. In addition, aluminum was present in the surface oxide, and a thin oxide layer rich in aluminum existed adjacent to the metal substrate. A similar, though not as evident, distribution of aluminum occurred in Incoloy 800. Incoloy 800 contains 0.38 wt % aluminum as compared with 1.5 wt % in CG-27. A thin, discontinuous aluminum-rich oxide layer near the oxide-metal interface and grain boundary oxides were previously noted for Sanicro 32. Titanium, at a concentration of 2.5 wt % in CG-27, appeared to be associated with aluminum in the oxide scales and as internally oxidized. In contrast, for the group III alloy W-545, which contains slightly more titanium (2.85 wt %) but much less aluminum (0.2 wt %), titanium does not preferentially oxidize.

The role of reactive elements such as yttrium, scandium, cerium, zirconium, and hafnium in improving oxide scale adherence particularly for Fe-Cr-Al, Ni-Cr-Al, and Co-Cr-Al alloys has been investigated in much detail [14-19]. The standard free energies of oxide formation of these reactive elements are more negative than those for iron, nickel, cobalt, chromium, and aluminum. Small additions (<1 at %) of these elements have been shown to dramatically improve oxide scale adherence and to reduce spalling in cyclic oxidation. The exact mechanism by which such an improvement occurs is not agreed upon by investigators in this field. For example, yttrium and scandium have been reported to increase oxide growth rates by forming rapid diffusion paths along yttria and scandia stringers [14]. Increased grain boundary transport of oxygen has been demonstrated by ^{18}O tracer studies on Ni-Cr-Al alloys with zirconium additions [15]. The resulting oxide adherence has been attributed [14,15,18] to (1) mechanical oxide pegging; (2) stress-strain accommodations at the oxide-matrix interface; (3) increased chemical bonding across the interface; and (4) a vacancy sink mechanism that precludes void formation at the oxide-metal interface, which would promote spalling.

It is postulated that for the alloys studied herein, aluminum plays a role similar to that of the reactive elements discussed previously. Aluminum has a more negative standard free energy of oxide formation than do the major alloying constituents of the candidate heater-head-tube alloys such as iron, nickel, and chromium. The internal aluminum oxidation suggests that controlling the inward oxygen diffusion plays a major role in the oxidation of CG-27 and probably Incoloy 800 [8]. Although the remaining group I alloys were not studied by electron microprobe techniques, the reactive elements niobium in N-155, niobium and aluminum in Inconel 718, and lanthanum in HS-188 probably play a role similar to that of aluminum in the two alloys that were examined. The results further suggest that although 0.4 wt % aluminum is adequate to be effective in promoting good scale adherence (Incoloy 800, Sanicro 32, Sanicro 31H, and Inconel 718), a concentration of 0.2 wt % aluminum such as exists for W-545, Fig. 9 and A-286 is insufficient to improve the oxidation behavior of these alloys. It is not clear from this study which of the previously suggested models for oxide scale adherence is to be preferred.

The factors effecting oxidation/corrosion behavior of the alloys is also important in minimizing hydrogen permeation through the tube walls. Formation of an adherent oxide film on the internal surface of the heater head tubes is required to reduce the hydrogen loss by permeation. Alloys with low oxidation/corrosion attack parameters, K_a also had low hydrogen permeability coefficients, ϕ . Results presented herein have clearly shown the importance of alloy composition, specifically the presence of the more reactive elements such as Al, Ti, and La as a key to controlling oxidation/corrosion behavior of the alloys. This, in turn, is reflected in the resulting microstructure where thin oxide layers containing the reactive

elements are desirable for long-life, low-hydrogen permeability heater head tube alloys.

Application of Results

Based on the results of these tests alloys CG-27, 12RN72, Sanicro 32, and Inconel 625 were selected for engine testing. Engine testing under accelerated conditions exceeded 2000 h or an equivalent 3300 h of urban-highway driving. Only alloy CG-27 did not fail by creep rupture in the engine test [20]. Alloy CG-27 has been selected as the heater head tube material for the automotive Stirling engine because of its good creep-rupture (endurance) strength, resistance to oxidation and corrosion, and resistance to hydrogen permeation as a result of forming a thin, tenacious oxide using CO₂ doped hydrogen.

Concluding Remarks

This study has shown that chemistry and microstructure of heater head tube alloys which develops during operation of the engine and in simulated tests play an important role in alloy selection for the automotive Stirling engine. Specifically the following features were shown to be important:

1. The presence of a sufficient amount (about 0.4 wt %) of the reactive metal aluminum in iron-base alloys leads to a microstructure characterized by a thin, adherent oxide scale rich in aluminum plus internal oxidation of aluminum which impedes inward diffusion of oxygen.

2. The thin, adherent oxide scales on both the combustion gas side and the CO₂ doped hydrogen side of the tubes act as barriers to hydrogen permeation.

3. The thin, adherent oxides characterized by no or very little spalling and metal loss lead to utilization of the full cross-sectional area of the tube alloy to provide the required strength for the 3500 hr life of an engine.

REFERENCES

1. Brogan, J.J., "Highway Vehicle Systems Program Overview," Highway Vehicle Systems Contractors Coordination Meeting, CONF-771037, Dept. of Energy, Washington, D.C., 1978, pp. 3-5.
2. Witzke, W.R., and Stephens, J.R., "Creep-Rupture Behavior of Seven Iron-Base Alloys After Long Term Aging at 760 °C in Low Pressure Hydrogen," NASA TM-81534, National Aeronautics and Space Administration, Washington, D.C., 1980.
3. Misencik, J.A., "Evaluation of Candidate Stirling Engine Heater Tube Alloys for 1000 Hours at 760 °C," NASA TM-81578, National Aeronautics and Space Administration, Washington, D.C., 1980.
4. Stephens, J.R., in Environmental Degradation of Engineering Materials in Hydrogen, M.R. Louthan Jr., R.P. McNitt and R.D. Sisson Jr., Eds., Virginia Polytechnic Institute and State University, Blacksburg, VA, 1981, pp. 123-132.
5. Schuon, S.R., and Misencik, J.A., "Effect of Oxide Films on Hydrogen Permeability of Candidate Stirling Engine Heater Head Tube Alloys," NASA TM-82824, National Aeronautics and Space Administration, Washington, D.C., 1982.
6. Misencik, J.A., "Evaluation of Candidate Stirling Engine Heater Tube Alloys at 820 °C and 860 °C," NASA TM-82837, National Aeronautics and Space Administration, Washington, D.C., 1982.
7. Stephens, J.R., Cronin, M.T., and Skog, E., in Proceedings of the Twentieth Automotive Technology Development, Contractors' Coordination Meeting, SAE P-120, Society of Automotive Engineers, New York, 1983, pp. 103-113.

8. Stephens, J.R., and Barrett, C.A., "Oxidation and Corrosion Resistance of Candidate Stirling Engine Heater-Head-Tube Alloys," NASA TM-83609, National Aeronautics and Space Administration, Washington, D.C., 1984.
9. Misencik, J.A., and Titran, R.H., "Evaluation of Candidate Stirling Engine Heater Tube Alloys After 3500 Hours Exposure to High Pressure Doped Hydrogen or Helium," NASA TM-83782, National Aeronautics and Space Administration, Washington, D.C., 1984.
10. Bhattacharyya, S., and Titran, R.H., Journal of Materials for Energy Systems, Vol. 7, No. 2, Sept. 1985, pp. 123-136.
11. Barrett, C.A., and Lowell, C.E., Journal of Testing and Evaluation, Vol. 10, No. 6, Nov. 1982, pp. 273-278.
12. Misencik, J.A., "Evaluation of Dopants in Hydrogen to Reduce Hydrogen Permeation in Candidate Stirling Engine Heater Head Tube Alloys at 760° and 820 °C," NASA TM-82920, National Aeronautics and Space Administration, Washington, D.C., 1982.
13. Stephens, J.R., in Sixteenth Summary Report, Highway Vehicle Systems Contractor's Coordination Meeting, CONF-7904105, Dept. of Energy, Washington, D.C., 1979, pp. 262-272.
14. Tien, J.K., and Pettit, F.S., Metallurgical Transactions, Vol. 3, No. 6, June, 1972, pp. 1587-1599.
15. Allam, I.M., Whittle, D.P., and Stringer, J., Oxidation of Metals, Vol. 13, No. 4, Aug. 1979, pp. 381-401.
16. Smialek, J.L., Journal of Electrochemical Society, Vol. 126, No. 12, Dec. 1979, pp. 2275-2276.
17. Khan, A.S., Lowell, C.E., and Barrett, C.A., Journal of the Electrochemical Society, Vol. 27, no. 3, Mar. 1980, pp. 670-679.
18. Barrett, C.A., Khan, A.S., and Lowell, C.E., Journal of the Electrochemical Society, Vol. 128, No. 1, Jan. 1981, pp. 25-32.

19. Reddy, K.P.R., Smialek, J.L., and Cooper, A.R., Oxidation of Metals, Vol. 17, Nos. 5/6, June 1982, pp. 429-449.
20. Skog, E., Cronin, M., and Stephens, J., in Proceedings of the Twenty-Second Automotive Technology Development Contractor's Coordination Meeting, SAE P-155, Society of Automotive Engineers, New York, 1985, pp. 175-180.

TABLE 1 -- CHEMICAL COMPOSITION OF COMMERCIAL ALLOYS

Alloy	Composition, wt %													
	Fe	Cr	Ni	Co	Mn	Si	Mo	Nb	W	Al	Ti	C	Other	
Iron-base alloys														
N-155	30	21	20	20	1.5	0.5	3.0	1.0	2.5	---	---	0.15	0.15N	
CG-27	38	13	38	--	.1	.1	5.5	.6	---	1.5	2.5	.05	.01B	
RA-330 ^a	43	19	35	--	1.5	1.3	---	---	---	---	---	.05	---	
Sanicro 32	43	21	31	--	.6	.47	---	---	2.8	.4	.4	.89	---	
Sanicro 31H	46	21	31	--	.6	.55	---	---	---	.4	.5	.07	.02N	
Incoloy 800	46	21	32	--	.75	.5	---	---	---	.38	.38	.05	---	
12RN72	47	19	30	--	1.7	.28	1.4	---	---	---	.5	.1	.02N	
A-286	53	15	26	--	1.4	.4	1.25	---	---	.2	2.15	.05	.26V	
W-545	54	14	26	--	1.5	.4	1.5	---	---	.2	2.85	.08	.08B	
Nitronic 40 ^a	64	21	6.5	--	9.0	---	---	---	---	---	---	.04	.30N	
253 MA	66	21	11	--	.4	1.7	.04	---	---	---	---	.09	.2N	
316 Stainless steel	66	18	13	--	2.0	1.0	2.5	---	---	---	---	.08	---	
19-9DL	67	19	9	--	1.1	.6	1.2	.4	1.2	---	.3	.3	---	
AL-EX-20 ^a	70	5	1.0	--	20	.42	---	---	---	3.15	---	.02	---	
Nickel-base alloys														
Inconel 750 ^b	8	16	71	--	0.16	0.23	---	0.05	---	0.72	2.5	0.05	---	
Inconel 625 ^b	3	22	61	--	.15	.3	9.0	4.0	---	.2	0.2	0.05	---	
Inconel 601 ^b	14	23	60	--	.5	.2	---	---	---	1.4	---	.05	---	
Inconel 718	18	18	53	--	.2	.3	3.1	5.0	---	.4	.9	.04	---	
Pyromet 901 ^b	34	12	45	--	.10	.19	5.9	---	---	---	2.6	.03	---	
Cobalt-base alloys														
HS-188	1.5	22	22	40	---	---	---	---	14	---	---	0.08	0.08La	

^aEvaluated in hydrogen permeability and endurance testing only.

^bEvaluated in oxidation/corrosion testing only.

TABLE 2 -- X-RAY DIFFRACTION DATA OF SPECIMEN SURFACE AFTER 3500-h TEST
 IN ORDER OF DECREASING INTENSITY
 [Values of d and a_0 are in nanometers.]

Rank	Alloy	Chromium content, wt %	1	2	3	4
1	HS-188	22	0.1818 Sesquioxide	$a_0 = 0.840$ Spinel	Mn_2O_3	0.408 (SiO_2)
2	Sanicro 31H	21	$a_0 = 0.840$	0.1819	SiO_2	$(Mn_{0.983}Fe_{0.017})_2O_3$
3	Inconel 718	18	$a_0 = 0.835$	0.1822	0.410(SiO_2)	-----
4	Inconel 800	21	$a_0 = 0.840$	0.1819	Mn_2O_3	0.409 (SiO_2)
5	N-155	21	$a_0 = 0.840$	0.1826	0.411(SiO_2)	0.272
6	CG-27	13	$a_0 = 0.835$ } Spinel	0.1821 } Sesquioxide	0.1841 Sesquioxide	Trirutile, d = 0.330
7	RA-330	19	$a_0 = 0.840$	0.1818	Mn_2O_3	-----
8	Sanicro 32	21	$a_0 = 0.840$	0.1819	SiO_2	$(Mn_{0.983}Fe_{0.017})_2O_3$
9	12RN72	19	$a_0 = 0.840$	0.1819	$(Mn_{0.983}Fe_{0.017})_2O_3$	SiO_2
10	253 MA	21	0.1839 Sesquioxide	$a_0 = 0.835$ Spinel	SiO_2	0.1812 Sesquioxide
11	A-286	15	$a_0 = 0.830$ Spinel	0.1813	NiO	-----
12	W-545	14	$a_0 = 0.840$ Spinel	0.1849 } Sesquioxide	-----	-----
13	316 Stainless steel	18	0.1842 Sesquioxide	0.1824	$a_0 = 0.845$ Spinel	Mn_2O_3
14	Nitronic 40	21	$a_0 = 0.840$ Spinel	0.1843	-----	-----
15	AL-EX-20	5	0.1839 Sesquioxide	$a_0 = 0.840$ Spinel	Mn_2O_3	-----
16	19-9DL	19	$a_0 = 0.840$ Spinel	0.1821 Sesquioxide	0.1843 Sesquioxide	-----

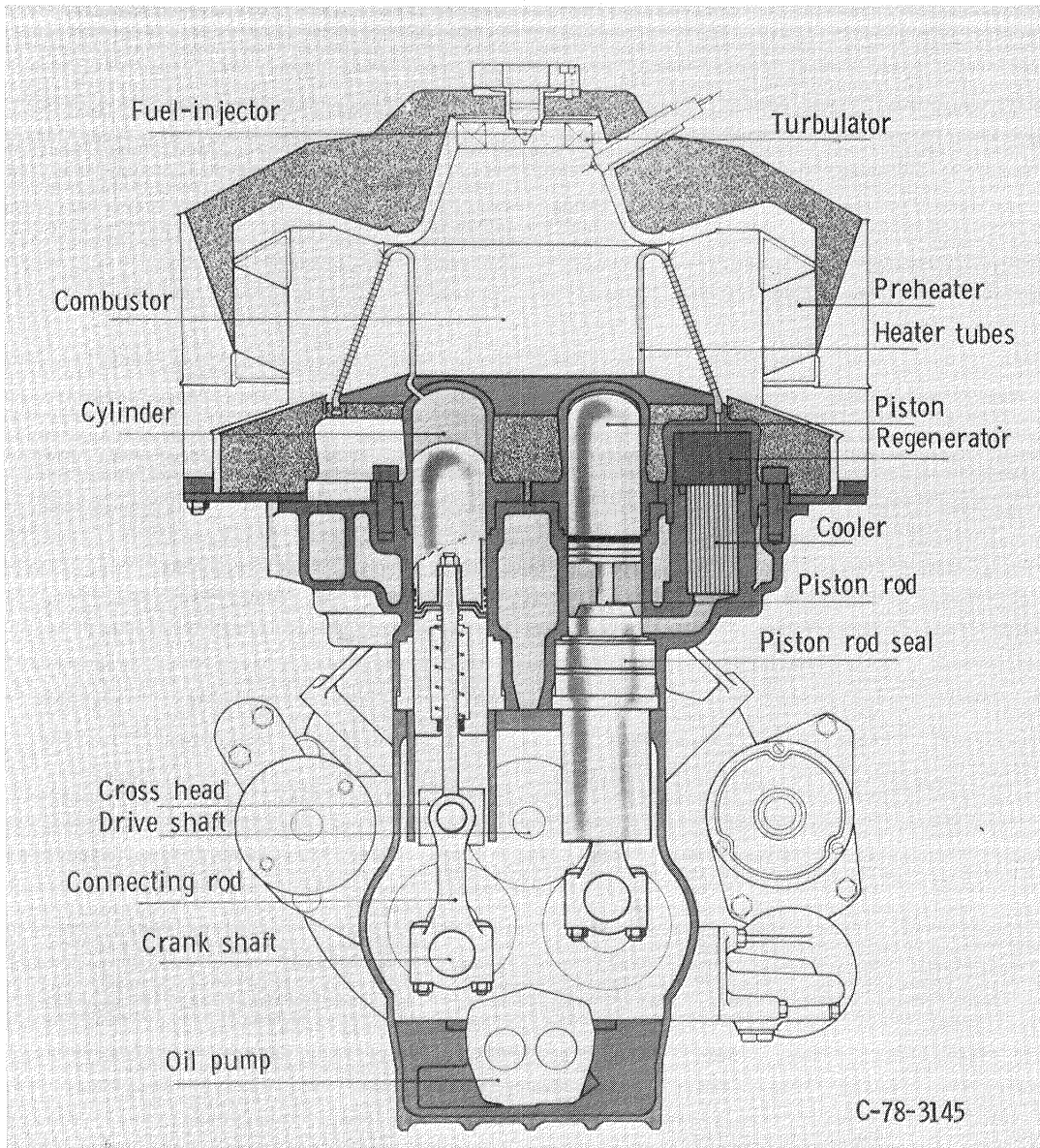


Figure 1. - Schematic representation of automotive Stirling engine.

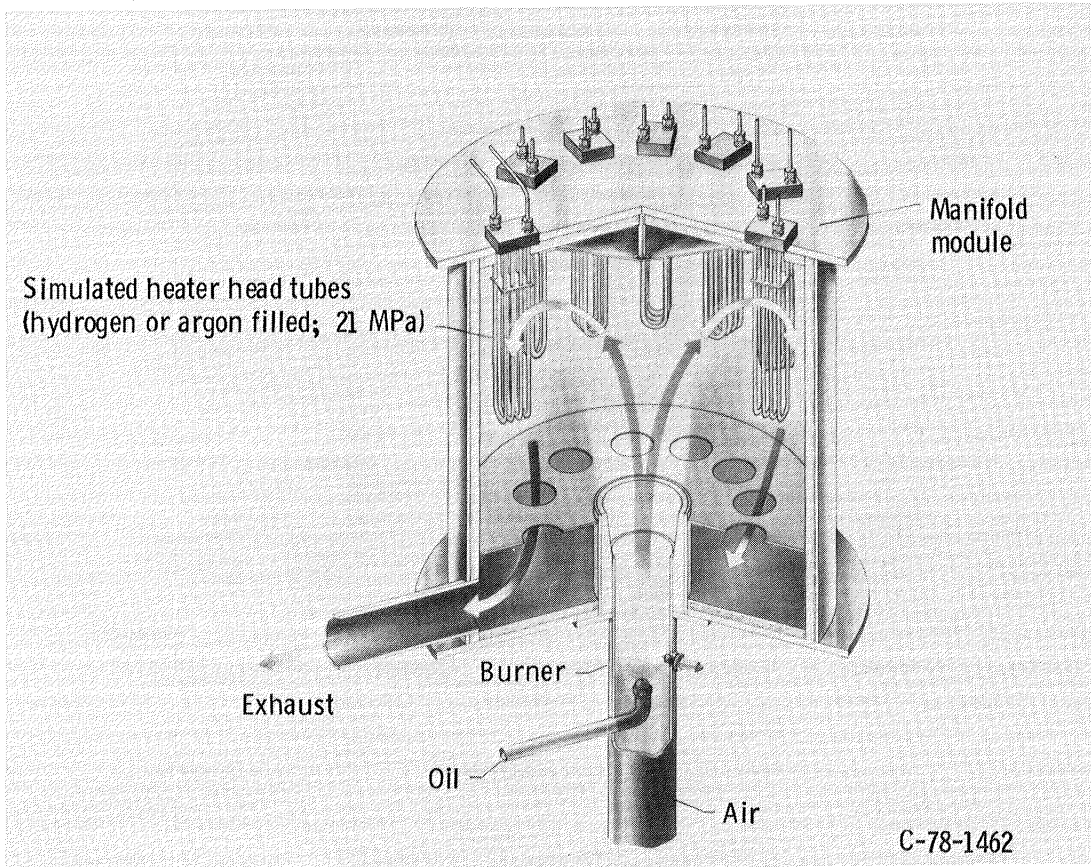


Figure 2. - Schematic representation of Stirling engine materials simulator test rig.

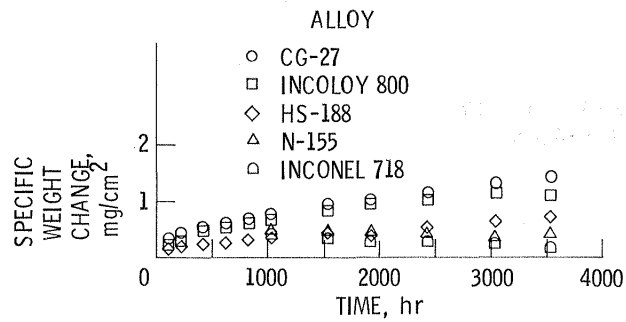


Figure 3. - Specific weight change data for group I alloys tested at 820 °C for 3500 hr.

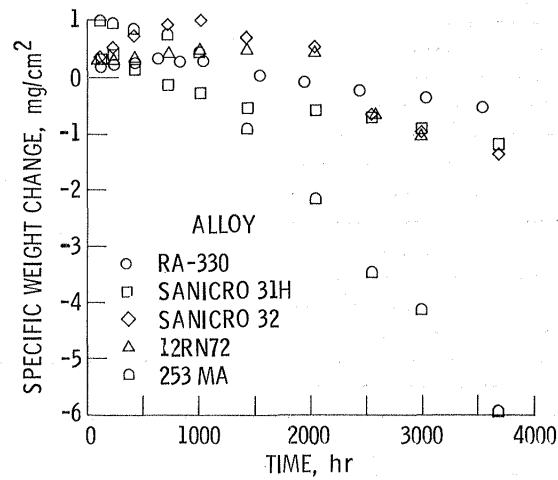


Figure 4. - Specific weight change data for group II alloys tested at 820 °C for 3500 hr.

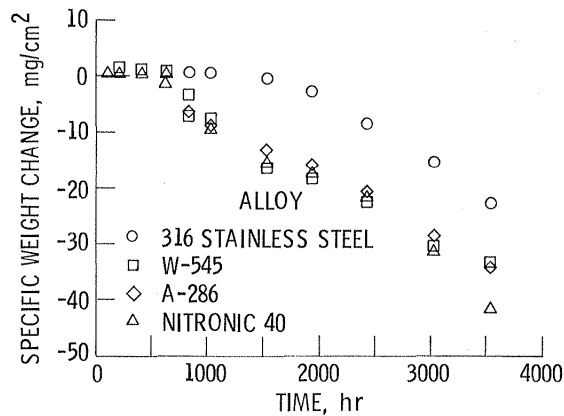


Figure 5. - Specific weight change data for group III alloys tested at 820 °C for 3500 hr.

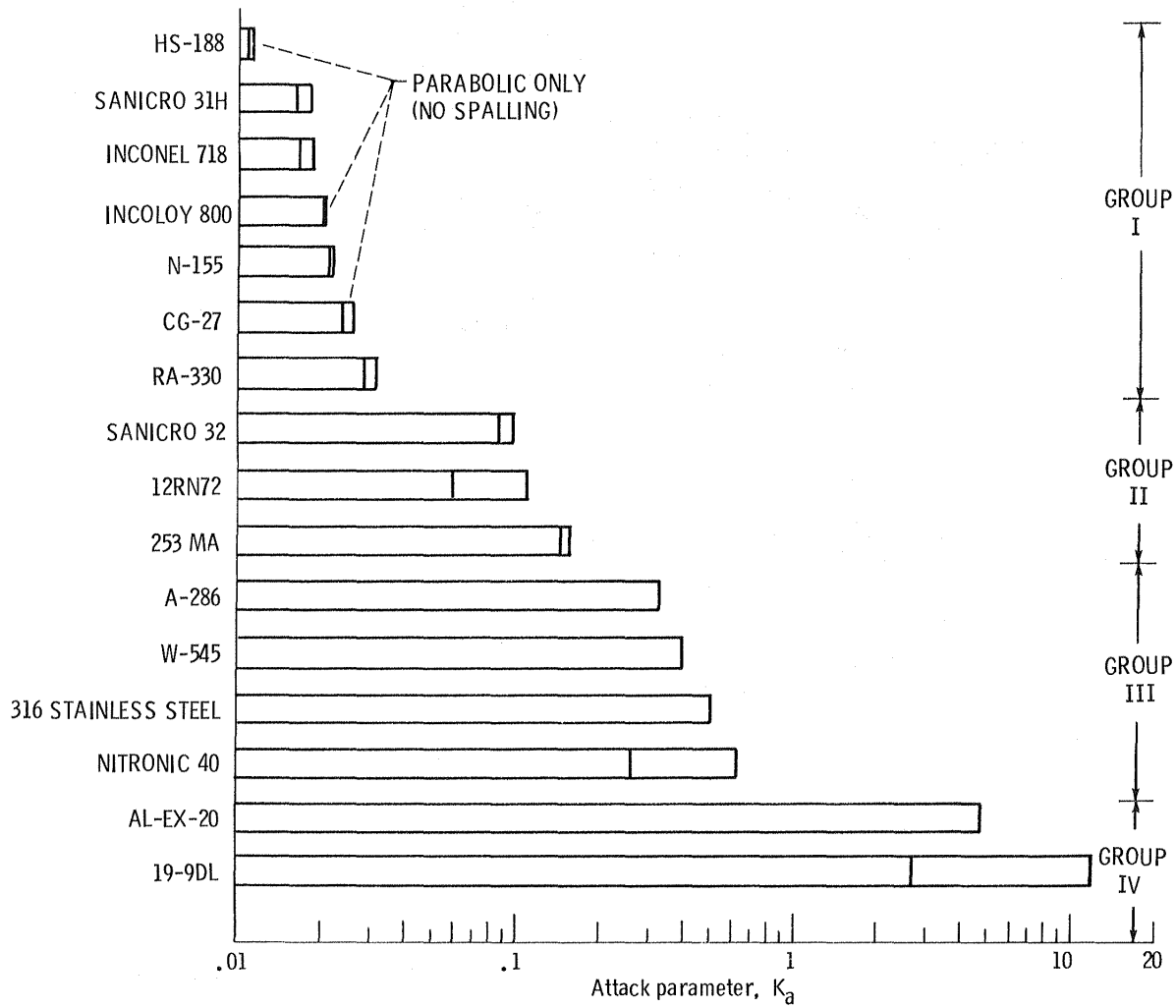
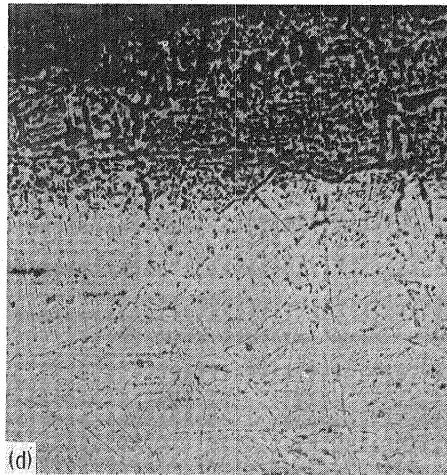
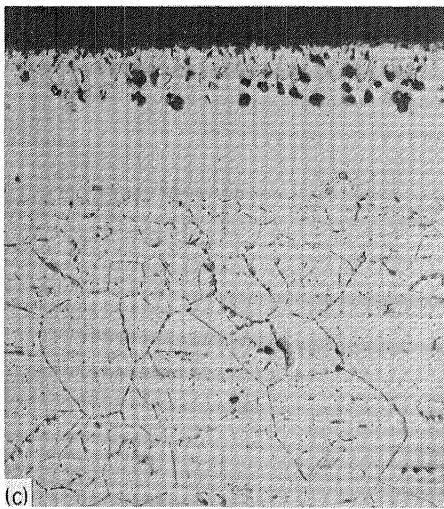
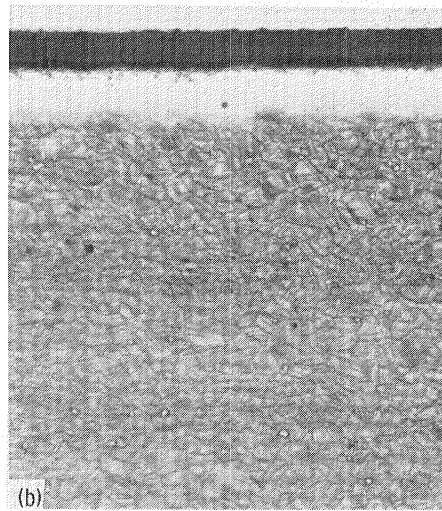


Figure 6. - Oxidation and corrosion attack parameter K_a for 3500-hr cyclic exposure in Stirling engine simulator rig. Temperature, 820°C ; cycles length, 5 hr; $K_a = k_1^{1/2} + 10k_2$. (Duplicate samples.)



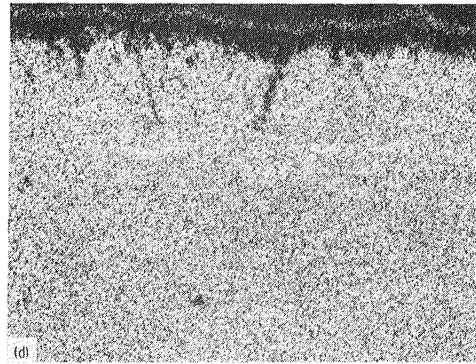
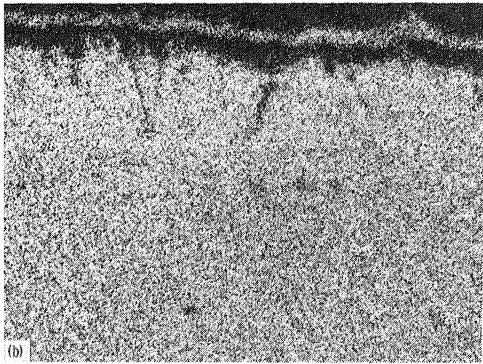
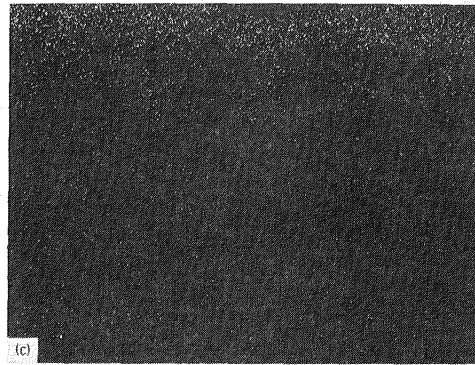
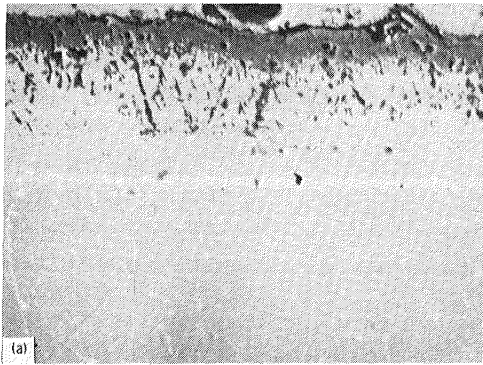
(a) CG-27.

(b) Inconel 718.

(c) Sanicro 32.

(d) W-545.

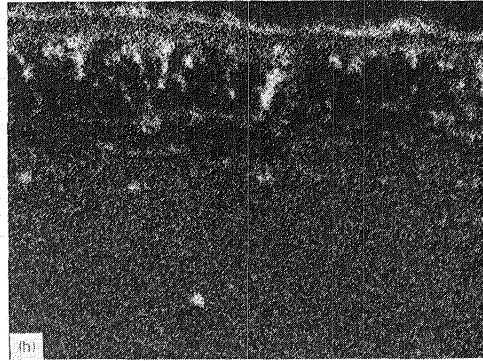
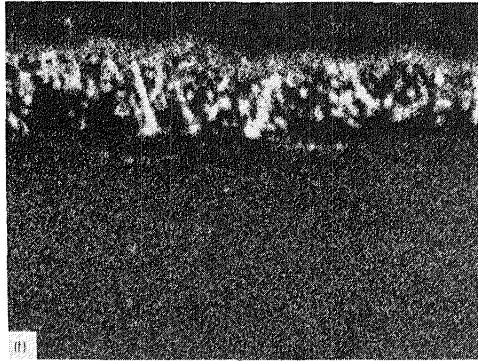
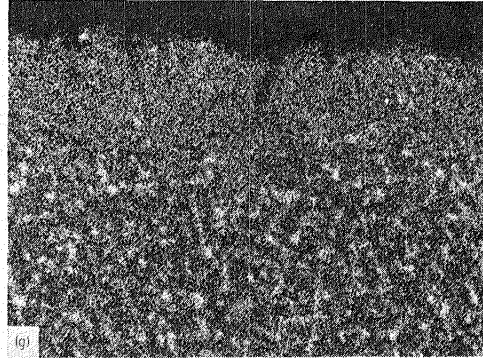
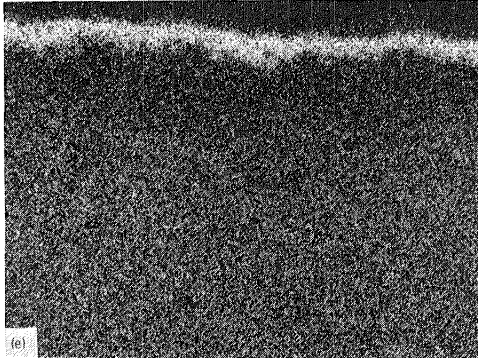
Figure 7. - Photomicrographs of selected 3500 hr oxidation and corrosion test specimens. Longitudinal view showing surface scales and depletion zones; magnification, 250.



(a) BSE.
(b) Iron.

(c) Oxygen.
(d) Nickel.

Figure 8. - Electron microprobe analyses of alloy CG-27. Magnification, 1000.



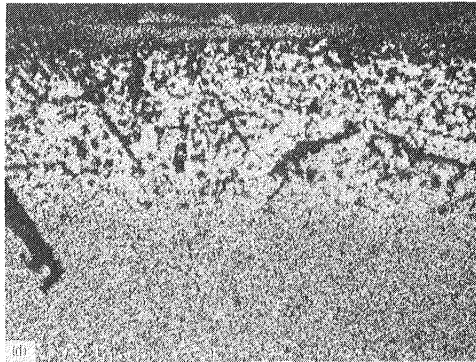
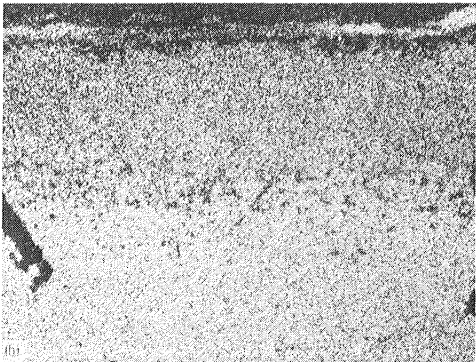
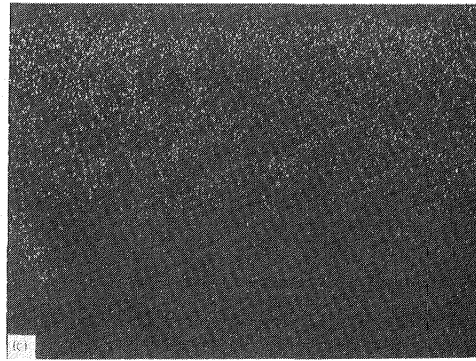
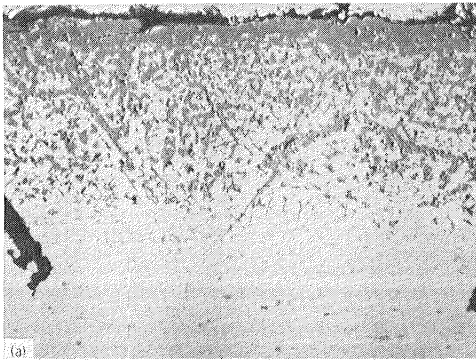
(e) Chromium.

(g) Molybdenum.

(f) Aluminum.

(h) Titanium.

Figure 8. - Concluded.



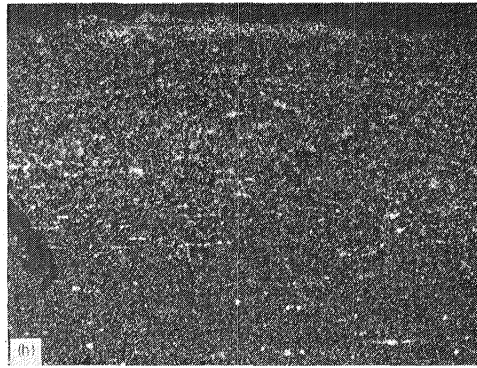
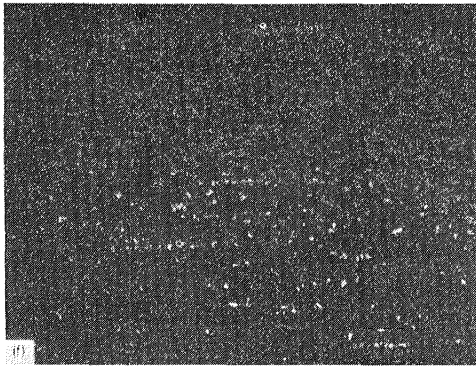
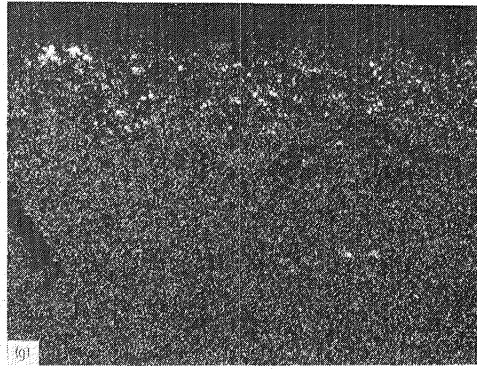
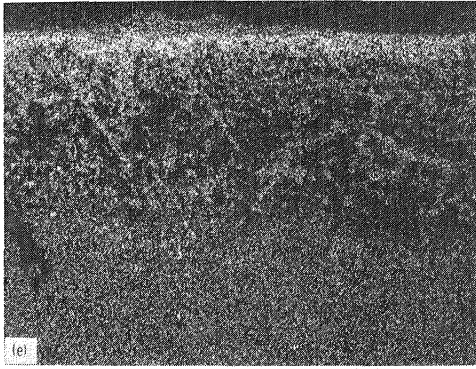
(a) BSE.

(b) Iron.

(c) Oxygen.

(d) Nickel.

Figure 9. - Electron microprobe analyses of alloy W-545. Magnification, 300.



(e) Chromium.
(f) Aluminum.

(g) Molybdenum.
(h) Titanium.

Figure 9. - Concluded.

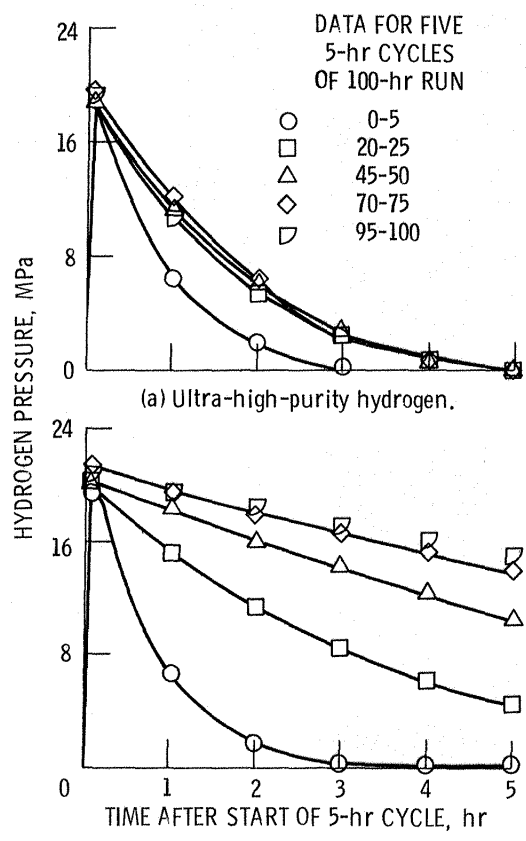


Figure 10. - Pressure decay curves for N-155 at 820 °C.

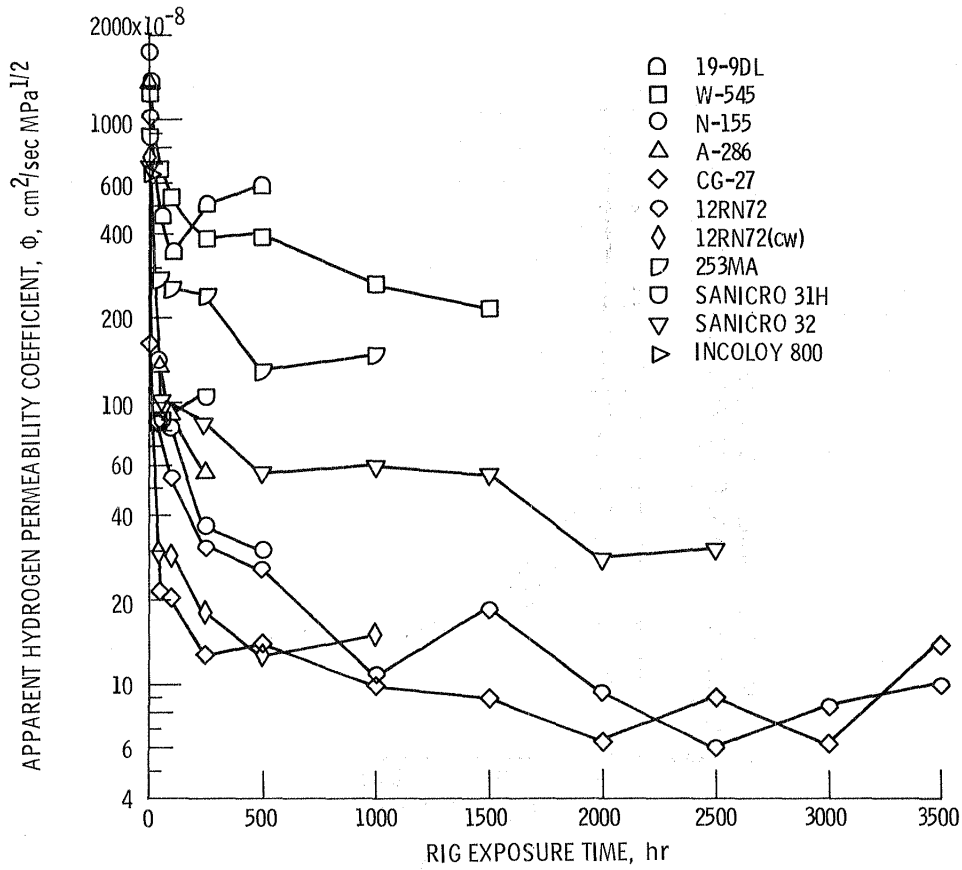


Figure 11. - Hydrogen permeability coefficient Φ versus rig exposure time for iron base alloys tested at 820 °C with $\text{H}_2 + 1\% \text{CO}_2$ at 15 MPa.

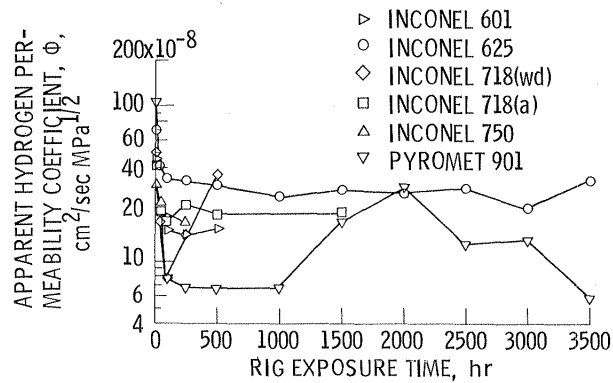


Figure 12. - Hydrogen permeability coefficient Φ versus rig exposure time for nickel base alloys tested at 820 °C with $\text{H}_2 + 1\% \text{CO}_2$ at 15 MPa.

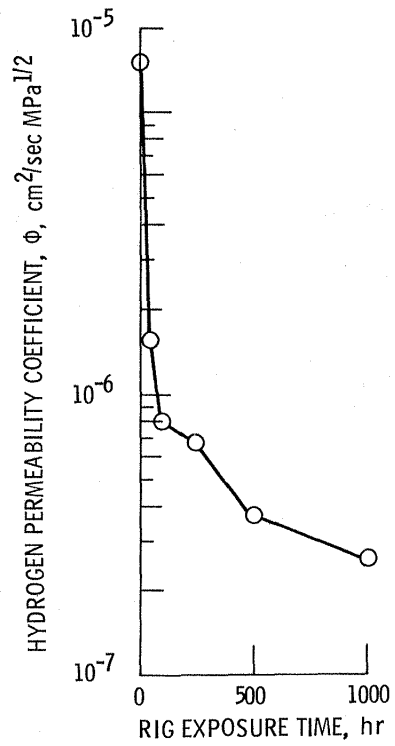


Figure 13. - Hydrogen permeability coefficient Φ versus rig exposure time for cobalt-base alloy HS-188 tested at 820 °C with H₂ + 1% CO₂ at 15 MPa.

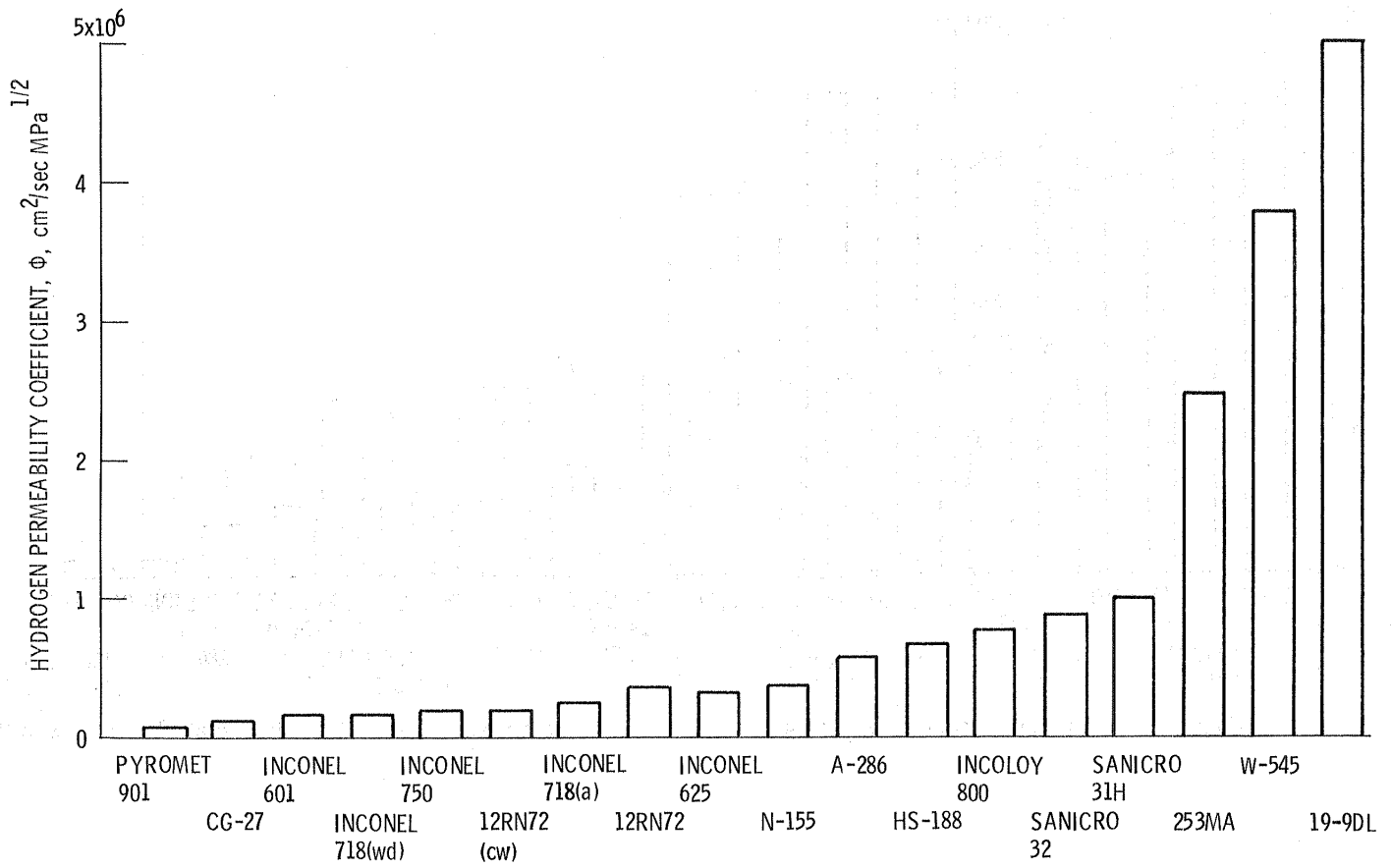


Figure 14. - Apparent hydrogen permeability coefficient at 250 hr for tubing material endurance tested at 820 °C and 15 MPa.

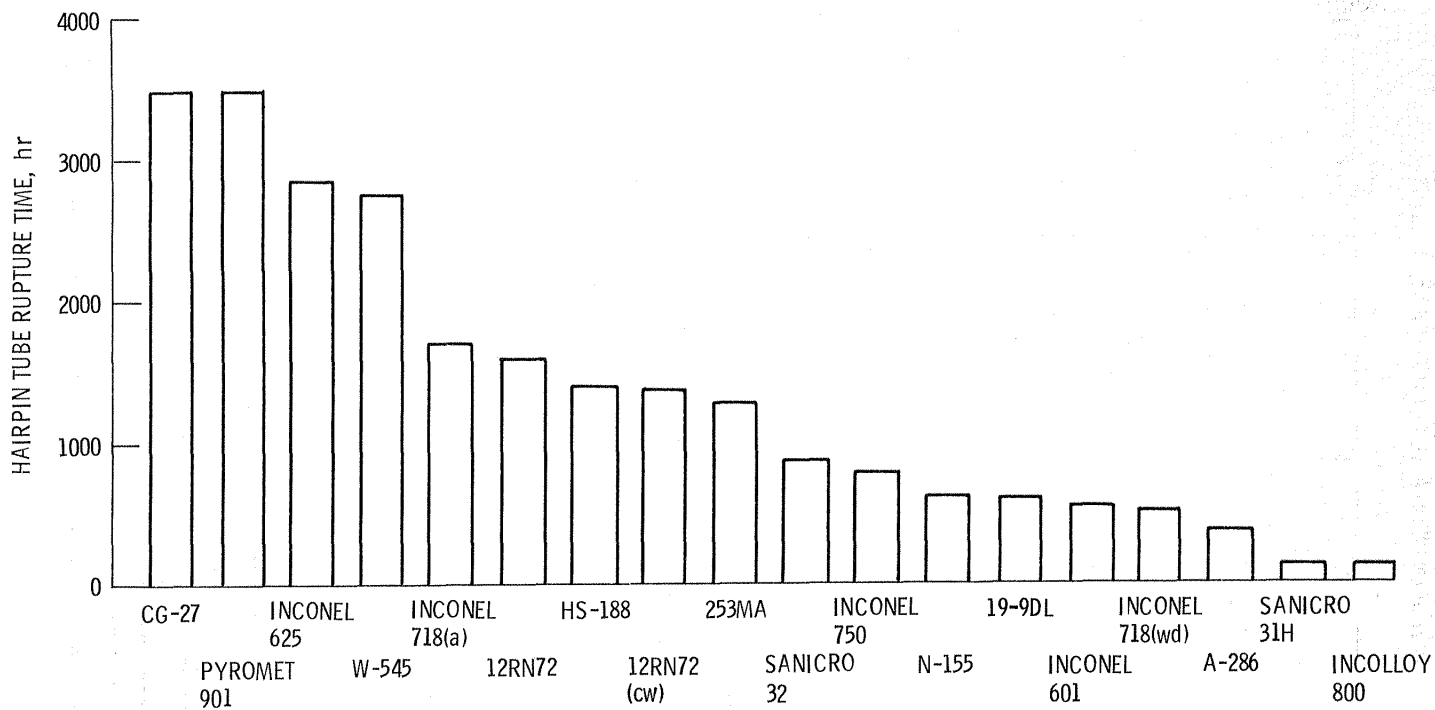
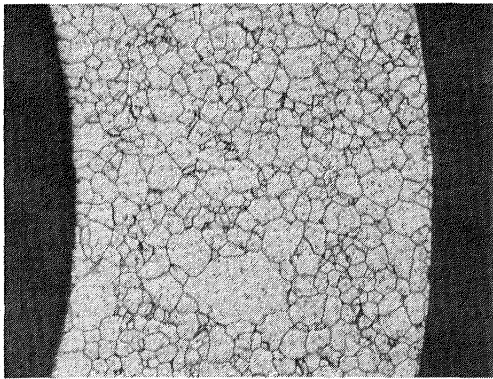
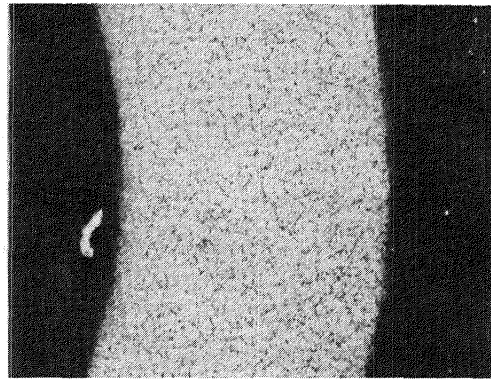


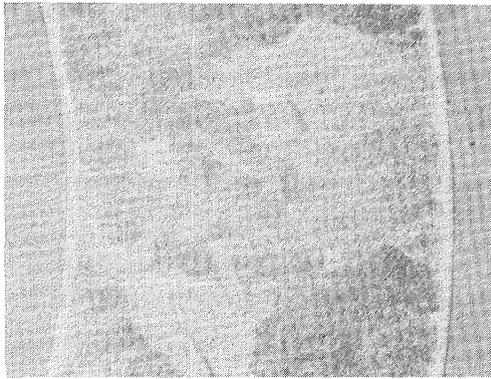
Figure 15. - Ranking of hairpin tubes according to rupture lives when pressurized with 15 MPa helium at 820 °C.



Unexposed

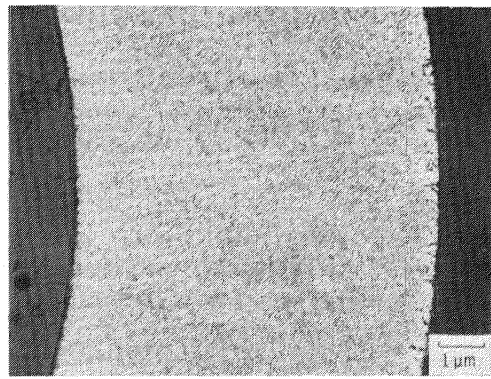


Unexposed



H₂ - 1% CO₂ exposed

(a) CG-27.



H₂ + 1% CO₂ exposed

(b) Inconel 625.

Figure 16. - Microstructures of hairpin tubes before and after rig exposure, 820⁰C, 3500 h.

1. Report No. NASA TM-87250		2. Government Accession No.		3. Recipient's Catalog No.	
4. Title and Subtitle Alloy Chemistry and Microstructural Control to Meet the Demands of the Automotive Stirling Engine				5. Report Date	
				6. Performing Organization Code 778-35-03	
7. Author(s) Joseph R. Stephens				8. Performing Organization Report No. E-2892	
				10. Work Unit No.	
9. Performing Organization Name and Address National Aeronautics and Space Administration Lewis Research Center Cleveland, Ohio 44135				11. Contract or Grant No.	
				13. Type of Report and Period Covered Technical Memorandum	
12. Sponsoring Agency Name and Address U.S. Department of Energy Office of Vehicle and Engine R&D Washington, D.C. 20545				14. Sponsoring Agency Code Report No. DOE/NASA/50112-63	
15. Supplementary Notes Final report. Prepared under Interagency Agreement DE-AI01-85CE50112. Prepared for the MiCon (Microstructural Control), sponsored by American Society for Testing Materials, Philadelphia, Pennsylvania, May 15-16, 1986.					
16. Abstract The automotive Stirling engine now under development by DOE/NASA as an alternative to the internal combustion engine, imposes severe materials requirements for the hot portion of the engine. Materials selected must be low cost and contain a minimum of strategic elements so that availability is not a problem. Heater head tubes contain high pressure hydrogen on the inside and are exposed to hot combustion gases on the outside surface. The cylinders and regenerator housings must be readily castable into complex shapes having varying wall thicknesses and be amenable to brazing and welding operations. Also, high strength, oxidation resistance, resistance to hydrogen permeation, cyclic operation, and long-life are required. A research program conducted by NASA Lewis focused on alloy chemistry and microstructural control to achieve the desired properties over the life of the engine. Results of alloy selection, characterization, evaluation, and actual engine testing of selected materials will be presented.					
17. Key Words (Suggested by Author(s)) Automotive Stirling engine; Iron-base alloys; Microstructure; Alloy composition; Hydrogen permeation; Oxidation; Corrosion			18. Distribution Statement Unclassified - unlimited STAR Category 26 DOE Category UC-25		
19. Security Classif. (of this report) Unclassified		20. Security Classif. (of this page) Unclassified		21. No. of pages	22. Price* A02

End of Document